Myod1 and GR coordinate myofiber-specific transcriptional enhancers

Daniela Rovito, Anna-Isavella Rerra, Vanessa Ueberschlag-Pitiot, Shilpy Joshi, Nezih Karasu, Vanessa Dacleu-Siewe, Khalil Ben Rayana, Kamar Ghaibour, Maxime Parisotto, Arnaud Ferry, et al.

Published online 9 April 2021

Myod1 and GR coordinate myofiber-specific transcriptional enhancers

Daniela Rovito[1,†], Anna-Isavella Rerra[1,†], Vanessa Ueberschlag-Pitiot[1,†], Shilpy Joshi[1], Nezih Karasu[1], Vanessa Dacleu-Siewe[1], Khalil Ben Rayana[1], Kamar Ghaibour[1], Maxime Parisotto[1], Arnaud Ferry[2], Scott A. Jelinsky[3], Gilles Laverny[1], Bruno P. Klaholz[1], Tom Sexton[1], Isabelle M. L. Billas[1], Delphine Duteil[1,*] and Daniel Metzger[1,*]

[1]Université de Strasbourg, CNRS UMR7104, INSERM U1258, IGBMC, F-67400 Illkirch, France, [2]Centre de Recherche en Myologie, UMRS974-Sorbonne Université-INSERM U974-Association Institut de Myologie, France and [3]Department of Inflammation and Immunology, Pfizer Research, Cambridge, MA, USA

ABSTRACT

Skeletal muscle is a dynamic tissue the size of which can be remodeled through the concerted actions of various cues. Here, we investigated the skeletal muscle transcriptional program and identified key tissue-specific regulatory genetic elements. Our results show that Myod1 is bound to numerous skeletal muscle enhancers in collaboration with the glucocorticoid receptor (GR) to control gene expression. Remarkably, transcriptional activation controlled by these factors occurs through direct contacts with the promoter region of target genes, via the CpG-bound transcription factor Nrf1, and the formation of Ctcf-anchored chromatin loops, in a myofiber-specific manner. Moreover, we demonstrate that GR negatively controls muscle mass and strength in mice by down-regulating anabolic pathways. Taken together, our data establish Myod1, GR and Nrf1 as key players of muscle-specific enhancer-promoter communication that orchestrate myofiber size regulation.

INTRODUCTION

Multicellular organisms owe their complexity to the capacity to generate and maintain various cell types sharing the same genetic blueprint. The establishment of cell identity is maintained through the spatio-temporal regulation of gene expression offered by a dynamic three-dimensional (3D) genome architecture (1). By coming in physical proximity to the promoter of their cognate target genes via the formation of chromatin loops (1–4), enhancers have emerged as key cis-regulatory elements that affect gene transcription regardless their orientation or distance from the transcription start site (TSS) of their nearest gene, thereby contributing to highly cell-specific transcriptomes. Chromosome conformation capture studies revealed that the genome is partitioned into topologically associating domains (TADs) (1), constrained at chromatin boundaries by focal interactions of cohesin-protein complexes and CCCTC–DNA-binding factor (Ctcf), one of the major architectural proteins shaping the 3D genome (5).

Ligand-activated transcription factors, such as nuclear receptors, are recruited to both enhancer and promoter regions in association with a large panel of coregulatory proteins that contribute to cell identity and specific responses to diverse signaling inputs. Despite the large number of comprehensive analyses of higher-order spatial genome folding, the identity of the molecular players that contribute to structural interactions to bridge temporally controlled and cell-type specific interactions remains to be fully characterized.

Skeletal muscle is a dynamic tissue that accounts for about one third of the body mass, and is essential for posture, locomotion and energy balance in mammals (6). In response to a variety of external stimuli, including mechanical load, nutritional status, inflammatory cytokines and hormones, the size of this tissue remodels through a dynamic balance between anabolic and catabolic processes to maintain muscle performance (7,8). The regulatory networks of myogenic commitment and differentiation programs involve a handful of distant located cis-regulatory modules in a highly-orchestrated chromosome rearrangement. However, gene regulation in skeletal muscle has only been partially uncovered at the genome-wide

level ([9–12](#)), and the underlying mechanisms remain poorly understood.

Using high-throughput sequencing-based analyses of histone modifications combined with assays for transposase-accessible chromatin with high throughput sequencing (ATAC-seq), we identified ∼ 27 000 active skeletal muscle-specific enhancers. We show that Myod1, a basic Helix-Loop-Helix (βHLH) transcription factor ([13,14](#)) that promotes a feed forward mechanism of gene transcription by binding to E-box sequences (5′-CANNTG-3′) ([15](#)), is one of the most prominent transcription factors bound at these enhancers. Remarkably, we uncovered that the glucocorticoid receptor [GR, NR3C1 ([16](#))], a ligand-dependent transcription factor belonging to the nuclear receptor superfamily, is associated with skeletal muscle enhancers in collaboration with Myod1. Using chromosome conformation capture on chip (4C) technology, we further show interactions between GR- and Myod1-bound myofiber-specific enhancers and the transcriptionally active promoter regions of glucocorticoid-responsive genes. These interactions take place in GC-rich regions to which the transcription factor Nrf1 is recruited. Our genome-wide analyses also revealed that GR in myofibers coordinates the expression of a large number of genes to downregulate anabolic pathways without affecting catabolic pathways at endogenous glucocorticoid levels. Taken together, our results provide in-depth insights into sophisticated epigenetic plasticity of gene regulation in skeletal muscles.

MATERIALS AND METHODS

Cell culture and transfection assays

C2C12 myoblasts, obtained from ATCC (CRL-1772), were grown in Dulbecco's modified Eagle's medium (DMEM), supplemented with 1 g/l glucose and 20% fetal calf serum. To induce myogenesis, cells were grown in DMEM, supplemented with 1 g/l glucose and 2% horse serum for 4 days. Two days before differentiation, C2C12 cells were transfected with 30 pmol siRNA against GR (5′-GCUUUGCUCCUGAUCUGAUUAUUAA-3′), Myod1 (5′-UUAUCAGGUGCUUUGAGAGAUCGAC-3′), Nrf1 (5′-CCACACACAGUAUAGCUCAUCUCGU-3′), or a scrambled control (5′-AGGUUCCGUGUACGUAAGACAAACU-3′) (Invitrogen) using Lipofectamine RNAimax (Invitrogen) according to the manufacturer's instructions. Cells were transfected again one day after myogenic induction.

Mice

Mice were maintained in a temperature- and humidity-controlled animal facility, with a 12-h light/dark cycle. Standard rodent chow (2800 kcal/kg, Usine d'Alimentation Rationelle, Villemoisson-sur-Orge, France) and water were provided *ad libitum*. Breeding and maintenance of mice were performed according to institutional guidelines. All experiments were done in an accredited animal house, in compliance with French and EU regulations on the use of laboratory animals for research. Intended manipulations were submitted to the Ethical committee (Com'Eth, Strasbourg, France) for approval and to the French Research

Ministry (MESR) for ethical evaluation and authorization according to the 2010/63/EU directive. Animals were killed by cervical dislocation, and tissues were immediately collected, weighed, and frozen in liquid nitrogen or processed for biochemical and histological analysis.

Generation of GR^{(i)skm−/−} mice

To selectively ablate GR in skeletal muscle myofibers, GR$^{L2/L2}$ mice, in which exon 3 (encoding part of the DNA binding domain) was flanked with two LoxP sites ([17](#)), were intercrossed with HSA-CreER^{T2} mice that express the CreER^{T2} recombinase selectively in skeletal muscle myofibers ([18](#)). All mice were on a C57/Bl6J background. Seven-week-old GR$^{L2/L2}$ control male mice and HSA-CreER^{T2}/GR$^{L2/L2}$ sex-matched somatic pre-mutant littermates were intraperitoneally injected with Tamoxifen (1 mg/mouse/day) for 5 days ([18](#)) to generate control (Ctrl) and GR$^{(i)skm−/−}$ mutant mice, respectively. Primers used for genotyping are listed in Supplementary Table S1.

Body lean and fat content

Body lean and fat content were recorded in anaesthetized mice by qNMR (PIXIMUS, GE Medical Systems) according to the manufacturer's instructions ([19](#)).

Muscle strength

A Grip Strength Meter (Bioseb) was used to measure forelimb and hindlimb grip strength ([19](#)). The test was repeated three consecutive times within the same session, and the mean value was recorded as the maximal grip strength for each mouse.

In situ isometric tibialis anterior muscle contraction in response to nerve stimulation was performed as described ([20](#)). In brief, tibialis distal tendons were attached to an isometric transducer (Harvard Bioscience). Sciatic nerves were proximally crushed and distally stimulated by a bipolar silver electrode using supramaximal square wave pulses of 0.1 ms. Data were analyzed on a microcomputer using a PowerLab system (4SP, AD Instruments).

Histological analysis

Immunofluorescence and Periodic acid–Schiff staining (PAS). Tissues were fixed in 10% buffered formalin and embedded in paraffin. Five μm paraffin sections were deparaffinized and rehydrated. For Periodic acid–Schiff staining, rehydrated tissue sections were treated with 0.5% periodic acid solution (Sigma-Aldrich, 3951), stained with Schiff's reagent (Sigma-Aldrich, 3952016), dehydrated and mounted. Immunofluorescence analysis was performed as described ([19,21](#)) with anti-GR (C-terminal, IGBMC, #3249) and anti-Pax7 (DSHB, AB_528428) antibodies. Mouse or rabbit IgGs were used as controls.

NADH staining. Cryosections (10 μm) were incubated with staining solution [0.2 M Tris pH 7.4, 1.5 mM NADH (Roche, 10128015001) and 1.5 mM nitroblue tetrazolium (Sigma-Aldrich, N-6876)], dehydrated in an ascending ethanol gradient, incubated twice with xylene and mounted as described ([19](#)).

Fiber cross-sectional area measurements

Muscle cross-sections were stained with dystrophin (ab15277, Abcam) to mark the sarcolemma surrounding each fiber, and cross-sectional area of gastrocnemius, soleus, quadriceps and tibialis muscles were quantified using the FIJI image-processing software as described (21). In brief, individual fibers were identified based on the intensity and continuity of the dystrophin-stained sarcolemma surrounding each fiber by segmentation. The area was measured after background subtraction, automated thresholding and analyzed with particles function of FIJI.

Blood glucose measurements and glucose tolerance test

Basal glucose levels were determined on 6 h-starved mice by blood collection from the tail vein.

Intraperitoneal glucose tolerance test (IPGTT) was performed after 6 h fasting. Following measurement of the basal glucose level (time 0), mice were intraperitoneally injected with 20% glucose in sterile saline solution (0.9% NaCl) at a dose of 2 g per kg body weight. Blood was collected from the tail vein after 15, 30, 45, 60, 90 and 120 min for glucose determination.

RNA extraction and analysis

Muscles and C2C12 cells were homogenized in TRIzol reagent (Life Technologies, Darmstadt, Germany). RNA was isolated using a standard phenol/chloroform extraction protocol, and quantified by spectrophotometry (Nanodrop, Thermo Fisher). cDNA was prepared by reverse transcription of 2 µg of total RNA using SuperScript IV (Life Technologies) and oligo(dT) primers according to the supplier's protocol. cDNA was diluted hundred times and quantitative PCR was performed with a Lightcycler 480 II (Roche) using the SYBR$^{\circledR}$ Green PCR kit (Roche) according to the supplier's protocol (2 µl cDNA, 4.8 µl H$_2$O, 5 µl Syber Green 2x mix and 0.2 µl of 100 µM primer mix). Primers are described in Supplementary Table S2. 18S, 36b4 and Gapdh were used as internal controls. Data were analyzed using the standard curve (22) and $\Delta\Delta$Ct methods (23). Primer efficiency was calculated as Eff = $100 \times 10^{((-1/\text{the slope value}) - 1)}$. As similar data were obtained with the various analyses, only results obtained with 18S housekeeping gene and the standard curve method are presented.

For RNA-seq, RNA integrity was confirmed by Bioanalyzer, cDNA library prepared, and sequenced by the standard Illumina protocol (HiSeq 4000, single-end, 50 bp) following the manufacturer's instructions. Image analysis and base calling were performed using RTA 2.7.7 and bcl2fastq 2.17.1.14. Adapter dimer reads were removed using DimerRemover. FastQC 0.11.2 (http://www.bioinformatics.babraham.ac.uk/projects/fastqc/) was used to evaluate the quality of the sequencing. Reads were mapped to the mouse mm10 genome (NCBI Build 38) using Tophat 2.1.1 (http://ccb.jhu.edu/software/tophat/index.shtml) (24) and Bowtie2 2.3.4.3 (http://bowtie-bio.sourceforge.net/bowtie2/index.shtml/) (25). Only uniquely aligned reads were retained for further analyses. Quantification of gene expression was performed using HTSeq 0.11.0

(26). For comparison among datasets, the transcripts with more than 50 raw reads were considered. Differentially expressed genes (DEGs) were identified using the Bioconductor libraries EdgeR and DESeq (27,28). A *P*-value $<10^{-5}$ and a fold change excluding values between 0.77 and 1.3 were used as a threshold for DEGs.

For microarray analysis, gene expression profiling was performed on total RNA isolated from gastrocnemius and soleus muscles of 9-week-old control and GR$^{(i)skm-/-}$ mice. Biotinylated single strand cDNA targets were prepared with the Ambion WT Expression Kit and the Affymetrix GeneChip$^{\circledR}$ WT Terminal Labeling Kit according to Affymetrix recommendations. Following fragmentation and end-labeling, cDNA was hybridized with GeneChip$^{\circledR}$ Mouse Gene 430 2.0 arrays (Affymetrix). Chips were washed, stained and scanned with the GeneChip$^{\circledR}$ Scanner 3000 7G (Affymetrix). Raw data CEL files were processed with Affymetrix Expression Console to calculate probe set signal intensities and the Robust Multi-array Average (RMA) algorithm with default settings was used for normalization. Differentially regulated genes were defined with fcros (29,30) (>50 signal units, *f*-value <0.025 or >0.975 for gastrocnemius; and >50 signal units, *f*-value <0.05 or >0.95 for soleus muscles) and further submitted for pathway analysis in WebGestalt (31) using the over-representation analysis (ORA) method and a significant level of FDR <0.05. Gene Ontology Enrichment analysis was also performed with WebGestalt. Heatmaps were generated by centering and normalizing expression values with Cluster 3.0 (32) and importing them to MultiExperiment Viewer (MeV, http://mev.tm4.org/#/welcome) (33). Genes were clustered according to the hierarchical method (HCL clustering) using gene tree, the Pearson correlation and average linkage.

Nuclei isolation

Nuclei were isolated from mouse skeletal muscle as described (34). In brief, muscles were homogenized in hypotonic lysis buffer [10 mM HEPES–KOH pH 7.3, 10 mM KCl, 5 mM MgCl$_2$, 0.1% NP-40, 0.1 M PMSF, protease inhibitor cocktail (45 µg/ml; Roche)]. For ChIP and 4C-seq experiments, lysates were fixed with 1% paraformaldehyde (PFA) for 10 min, and incubated for additional 10 min with 125 mM glycine. Sample was further homogenized with a loose dounce, and centrifuged at 1000 g for 5 min at 4°C. Pellets were resuspended in 5 ml ice-cold hypotonic buffer, filtered through 70 µm and 40 µm cell strainers, and centrifuged at 1000 g for 5 min at 4°C to obtain nuclei. For ATAC-seq and co-immunoprecipitation experiments, a similar procedure was applied without PFA fixation.

To isolate nuclei from differentiated C2C12 cells, myotubes were fixed with 1% PFA for 10 min. PFA reaction was quenched with 125 mM glycine for 5 min. Cells were harvested and washed twice with ice-cold PBS. Cell pellets were incubated with cytosolic buffer [10 mM HEPES, 60 mM KCl, 1 mM EDTA, 0.075% (v/v) NP40, 1 mM DTT and 1 mM PMSF (pH 7.6) containing protease inhibitors (Roche)], and incubated on ice for 8 min. After centrifugation at 400 g for 5 min, nuclei were washed in PBS and incubated on ice with 1% SDS-sonication buffer (50 mM

Tris, pH 8.1, 10 mM EDTA, 1% SDS containing protease inhibitors).

Chromatin immunoprecipitation

Chromatin immunoprecipitation (ChIP) followed by qPCR analysis (ChIP-qPCR) was assessed on skeletal muscle or C2C12 myotube nuclear extracts as described (34), using anti-GR (C-terminal, IGBMC, #3249), anti-Nrf1 (Abcam, ab55744), anti-Myod1 (Cell signaling, 13812), or anti-Myog (Santa Cruz, SC576) antibodies, or a mouse or a rabbit IgG negative control on protein G-Sepharose 4B (GE Healthcare) (35). Primers used for ChIP-qPCR are described in Supplementary Table S3.

For ChIP-seq analysis, libraries were prepared from AR- (C-terminal, IGBMC, #3299), GR- (C-terminal, IGBMC, #3249), H3K27ac- (Active Motif, 39133), H3K27me3- (Active motif, 39155), H3K4me3- (Abcam, 1012-100), H3K4me1- (Active Motif, 39297), Polr2- (Santa Cruz H-224, SC9001) and Ctcf- (Sigma-Aldrich, 07–729) immunoprecipitated DNA from skeletal muscle nuclear extracts as described (34). ChIP-seq libraries were sequenced with an Illumina Hiseq 4000 as paired-end 100 bp reads for Ctcf and H3K4me3 or single-end 50 bp reads for the other sequencing datasets, and mapped to the mm10 reference genome using Bowtie 2 (25). Uniquely mapped reads were retained for further analysis. MACS2 algorithm (https://github.com/taoliu/MACS/) (36) was used for the peak calling with non-immunoprecipitated chromatin as control. All peaks with a FDR >0.01 were excluded from further analysis. The genome-wide intensity profiles were visualized using the IGV genome browser (http://software.broadinstitute.org/software/igv/) (37). HOMER was used to annotate peaks and for motif searches (38). Genomic features (promoter/TSS, 5′ UTR, exon, intron, 3′ UTR, TTS and intergenic regions) were defined and calculated using Refseq and HOMER according to the distance to the nearest TSS. Clustering analyses were done with the seqMINER software (39), and clustering normalization was done with the K-Means linear option. Venn diagrams were generated with Venny (40) or InteractiVenn (41). Additional binding site analyses were performed using the MEME Suite (42). *De novo* identified motifs were referred to as follow: R = purine (G or A); Y = pyrimidine (T or C). Further bioinformatics analyses were performed with bedtools (https://bedtools.readthedocs.io/en/latest/index.html) (43): fasta sequences were obtained from bed files with GetFastaBed, location intersections were performed with Intersect interval and Multiple intersect, and gene centric analyses of peak distribution were performed with WindowBed.

ATAC-seq

ATAC-seq libraries were generated as described (44) with some modifications. For Transposition Reaction, 50 000 nuclei from murine skeletal muscles were incubated with 25 μl of TD reaction buffer and 2.5 μl of Tn5 Transposase reaction mix (Nextera index kit FC-121–1030, Illumina, San Diego, CA, USA) for 30 min at 37°C. To generate multiplexed libraries, the transposed DNA was initially amplified for 10 PCR cycles using 2.5 μl each of 25 μM PCR Primer 1 and 2.5 μl of 25 mM Barcoded PCR Primer 2 from the Nextera index kit, 25 μl of NEBNext High-Fidelity 2× PCR Master Mix (New England Biolabs, Boston, MA, USA) in a total volume of 50 μl. After the reaction, transposed DNA was purified using a Qiagen MinElute PCR Purification Kit (Qiagen) and used for subsequent PCR amplification. Five microliters of the amplified DNA was used to determine the appropriate number of additional PCR cycles using qPCR. The additional number of cycles was calculated through the plotting of the linear Rn versus cycle, and corresponds to one-quarter of the maximum fluorescent intensity. Amplification was performed on the remaining 45 μl of the PCR reaction using the 18 additional cycles. The amplified fragments were further purified two times with AMPure XP beads. The size distribution of the libraries was assessed on Bioanalyzer with a DNA High Sensitivity kit (Agilent Technologies, Santa Clara, CA, USA), and the concentration was measured with Qubit DNA High Sensitivity kit in Qubit 2.0 Flurometer (Life Technologies, Carlsbad, CA, USA).

Libraries were multiplexed and sequenced as 50 bp paired-end reads on an Illumina Hiseq 4000 instrument. Image analysis and base calling were performed using RTA 2.7.3 and bcl2fastq 2.17.1.14. Adapter dimer reads were removed using DimerRemover. Raw fastq reads were first evaluated using FastQC (www.bioinformatics.babraham.ac.uk/projects/fastqc) before continuing. For each library, raw .fastq reads were aligned using Bowtie2 version 2.3.4.3 to the mm10 reference genome. Chromatin accessibility peaks were called using MACS2 using custom parameters (–nomodel –broad –shift -100 –extsize 200 –keep-dup all –qvalue 0.05) (36). Downstream processing of sequencing data was performed using Samtools (http://samtools.sourceforge.net/) (45).

4C-seq experiments

Thymus from 4-week-old mice was dissected, minced in PBS and mechanically dissociated in a 10 ml syringe. Thymus homogenate was washed and filtered in PBS, and Double positive (DP) thymocytes were sorted by FACS with anti-CD4-PE (eBioScience, 12-0043-82) and anti-CD8a-FITC antibodies (eBioScience, 11-0086-42). Five millions of permeabilized DP thymocyte or skeletal muscle nuclei were incubated overnight with the DpnII restriction enzyme, and DNA segments were ligated with T4 DNA ligase as described (46). Reverse cross-linked and purified DNA was digested with Csp6I and circularized by T4 DNA ligase. Fifty ng of purified DNA were used as a template for PCR with bait-specific primers (Supplementary Table S4) containing Illumina adapter termini. PCR reactions were pooled and, after primer removal with 1.8x AMPure XP beads, DNA was sequenced with a HiSeq 4000 (Illumina) as single-end 50 bp reads. Sequences were trimmed to remove primer and bait fragment sequence with the sabre tool (https://github.com/najoshi/sabre), mapped to the genome with Bowtie and converted to restriction fragment space as described (47). Interactions were called on single 4C experiments with peakC (48), using a sliding window of 21 fragments.

Genomic distribution of peaks

The mm10 RefSeq Genes annotation available from the UCSC table browser was used to define all genomic features except enhancers. Multiple TSSs of genes were included in the analysis. Enhancers were defined by mapping H3K27ac, H3K4me1 and H3K4me3 bam files on H3K27ac peaks.

Bioinformatics parameters

Parameters were set as default, with the exception of the following:

RNA-seq:
DimerRemover parameters: -a AGATCGGAAGAGCA-CACGTCTGAACTCCAGTCAC
Bowtie2 parameters: –very-fast-local
Tophat2 parameters: –read-realign-edit-dist 1000 –read-edit-dist 2 –library-type FR First Strand –read-mismatches 2
HTSeq parameters: –mode intersection-nonempty –stranded reverse –minaqual 10 –type exon –idattr gene_id
Deseq2 R script: commands as they appear in the vignette of Deseq2
edgeR R script: commands as they appear in the vignette of edgeR
ChIP-seq:
Bowtie parameters: –very-fast-local
MACS2 parameters: callpeak – gsize 1.87e9 –format BAMPE – bw 300 – qvalue 0.01 –nolambda – mfold [5; 50] – slocal 1000 –llocal 10000 –broad (only for broad peak calling)
MEME-ChIP website parameters: –motif discovery and enrichment mode classic mode –sequence alphabet DNA, RNA or Protein – input the motifs Jaspar Core, Vertabrates, UniPROBE Mouse – MEME options count of motifs 5 width of motif 6–15
Homer parameters: -len 15
seqMINER: run java -Xmx8000m -jar seqMINER.jar when using Atac-seq bam files.

Protein analysis

Western blot analyses. Muscles were homogenized in RIPA buffer [50 mM Tris pH 7.5, 1% Nonident P40, 0.5% Sodium Deoxycholate, 0.1% SDS, 150 mM NaCl, 5 mM EDTA, 1 mM PMSF and protease inhibitor cocktail (45 μg/ml; Roche)]. Homogenates were separated in polyacrylamide gels and blotted to Hybond nitrocellulose membranes (Amersham Biosciences). Membranes were decorated using the following antibodies: anti-AR (C-terminal, IGBMC, #3299), anti-GR (C-terminal, IGBMC, #3249, 1/500), anti-Pi3 kinase p85 (ab71925, Abcam, 1/500), anti-Ddit4 (10638-1-AP, Proteintech, 1/500), Akt3 (14982, Cell Signaling, 1/200), anti-phospho-mTOR (Ser2448, 5536, Cell Signaling, 1/1000), anti-mTOR (2983, Cell Signaling, 1/500), anti-phospho-4E-BP1 (Thr37/46, 2855, Cell Signaling, 1/1500), anti-4E-BP1 (9644, Cell Signaling, 1/1500), anti-4E-BP2 (2845, Cell Signaling, 1/200), anti-phospho-FOXO1 (Ser256, 9461, Cell Signaling, 1/1000), anti-FOXO1 (2880, Cell Signaling, 1/1000), anti-phospho-FOXO3a (Ser318/321, 9465, Cell Signaling, 1/1000), anti-FOXO3a (2497, Cell Signaling, 1/1000), total OXPHOS rodent WB antibody cocktail (ab110413, Abcam, 1/1000), anti-beta-Tubulin (IGBMC, 1Tub2A2, 1/5000), anti-Nrf1 (ab55744, Abcam, 1/500), anti-Myod1 (Cell Signaling, 13812, 1/200), anti-Vinculin (H-10, SC25336, Santa Cruz) and anti-Gapdh (clone 6C5, MAB374, Millipore; or #2118, Cell Signaling, 1/10000). Secondary antibodies conjugated to horseradish peroxidase (Jackson ImmunoResearch, 1/10000) were detected using an enhanced chemiluminescence detection system (ECLplus, GE Healthcare) and an ImageQuant LAS 4000 biomolecular imager (GE Healthcare). Protein quantification was assessed by the FIJI/ImageJ distribution software (https://imagej.net/ImageJ) (49).

Immunoprecipitation assays. 200 μg of muscle nuclear extracts were incubated with 5 μg of anti-GR (C-terminal, IGBMC, #3249), anti-Myod1 (13812, Cell Signaling) or anti-Myog (SC576, Santa Cruz) antibodies, or rabbit IgG, and processed for Western bot analyses. Membranes were incubated with mouse anti-rabbit IgG (L27A9 Conformation Specific, Cell signaling, 1/5000) for 1 h at room temperature before addition of the secondary antibodies following manufacturer's instructions.

Recombinant protein expression and purification

The cDNA encoding the human GR DNA binding domain (DBD; A412-G506), cloned in the pETite vector encoding a N-terminal His6 coupled to a SUMO fusion protein (Lucigen Corp.), was expressed in *E. coli* BL21 (DE3) pRARE, by 0.1 mM isopropyl-β-d-thiogalactopyranoside (IPTG) induction at 18°C overnight. Bacteria were resuspended in 20 mM Tris–HCl pH 8, 400 mM NaCl, 5% glycerol, 4 mM 3-[(3-cholamidopropyl)dimethylammonio]-1-propanesulfonate hydrate (CHAPS), 2 mM tris(2-carboxyethyl)phosphine hydrochloride (TCEP), 20 mM imidazole, and a protease inhibitor cocktail, sonicated and centrifuged. The supernatant was loaded on a HisTrap FF crude column (GE Healthcare). Proteins were eluted at 250 mM imidazole, dialyzed in imidazole-free buffer in the presence of SUMO protease (1 U/1000 μg protein), loaded on a Heparin prepacked column (GE Healthcare), eluted with a salt gradient (20–1000 mM) and further purified by size exclusion chromatography on Superdex S75 (16/60 and 10/300, GE Healthcare) using 10 mM HEPES–KOH pH 7.5, 150 mM KAc, 3 mM MgAc and 1 mM TCEP buffer. Protein samples were concentrated using Amicon-Ultra centrifugal filter units (Millipore).

Strep-tagged human GR protein (amino-acids 1–777) was expressed in SF9 insect cells in the presence of 10 μM dexamethasone for 48 h. Cells were harvested and resuspended in 20 mM Tris–HCl pH 8.0, 400 mM NaCl, 5% glycerol, 4 mM CHAPS, 4 mM TCEP, 10 μM triamcinolone acetonide and a protease inhibitor cocktail. After sonication, the lysate was centrifuged to collect the soluble fraction, which was incubated at 4°C during 2 hours with Streptactin beads (IBA). Proteins were eluted with the same buffer supplemented with 5 mM desthiobiotin. After concentration using 50 kDa cutoff Amicon-Ultra centrifugal filter units (Millipore), GR was further purified by size

exclusion chromatography on Superdex 200 10/300 (GE Healthcare) using 20 mM HEPES–KOH pH 7.5, 400 mM NaCl, 3 mM $MgCl_2$, 1 mM TCEP and 10% glycerol buffer.

His-tagged mouse Myod1 protein (amino-acids 1–318) was expressed in *E. coli* BL21(DE3) by IPTG induction. Cells were resuspended in 50 mM Tris–HCl pH 8, 300 mM NaCl, 10% glycerol, 1 mM CHAPS, 1 mM TCEP, 20 mM imidazole and a protease inhibitor cocktail. After sonication, the lysate was centrifuged, and the soluble fraction was collected and loaded on a Histrap column (GE Healthcare). Proteins were eluted over an imidazole gradient. After dialysis, Myod1 was concentrated using 30 kDa cutoff Amicon-Ultra centrifugal filter units (Millipore), and purified on a Superdex 200 10/300 (GE Healthcare) using 20 mM HEPES–KOH pH 7.5, 400 mM NaCl, 3 mM $MgCl_2$, 1 mM TCEP and 10% glycerol buffer.

His-tagged human TIF2 polypeptide (amino-acids 623–773) was expressed in *E. coli* BL21(D3) by IPTG induction. After harvesting, cells were resuspended in 20 mM HEPES pH 8.0, 60 mM NaCl, 60 mM KCl, 5 mM $MgCl_2$, 1 mM CHAPS, 10% glycerol, 1 mM TCEP and a protease inhibitor cocktail. After sonication, the lysate was centrifuged and the soluble fraction was collected and loaded on a Histrap column (GE Healthcare). The hTIF2 fragment was eluted over an imidazole gradient, concentrated using a 3 kDa cutoff Amicon-Ultra centrifugal filter units (Millipore) after dialysis against the imidazole-free buffer, and purified on a Superdex 200 10/300 (GE Healthcare) using 20 mM HEPES–KOH pH 7.5, 400 mM NaCl, 3 mM $MgCl_2$, 1 mM TCEP and 10% glycerol buffer.

Microscale thermophoresis

Microscale thermophoresis (MST) was performed as described (50). The apparent Kd value of the GR DBD bound to DNA was measured using a Monolith NT 115 from NanoTemper Technologies GmbH. Recombinant purified GR DBD was labelled with the fluorescent dye NT-647 (NanoTemper Technologies) using the Monolith NTTM Protein Labelling kit (amine reactive). The labelling procedure and the subsequent removal of free dye were performed within 1 hour. Unlabeled DNA was serially diluted from a concentration of 100 μM to 1 nM in the presence of 1667 nM labelled receptor, and loaded into Premium capillaries (NanoTemper Technologies reference MOK025). Measurements were performed at 20°C in 10 mM Hepes KOH pH 7.4, 150 mM KOH, 3 mM MgAc, 1 mM TCEP, and 1% BSA, at 50% LED power and 20% IR-laser power. Data were analyzed using the MO Affinity Analysis v2.3 software (https://nanotempertech.com/monolith-mo-control-software/).

In vitro pull-down assay

One nmol of recombinant human GR was incubated at 4°C with 50 μl of streptactin beads pre-equilibrated in the size exclusion chromatography buffer. After 1 h, the flowthrough was collected by centrifugation at 500 g, and beads were washed with 20 mM HEPES–KOH pH 7.5, 250 mM NaCl, 3 mM $MgCl_2$, 1 mM TCEP and 10% glycerol buffer. 2.5 nmol of recombinant Myod1 or hTIF2 fragment were incubated with beads at 4°C for 1 h. Beads were

washed, proteins were eluted with 5 mM desthiobiotine and loaded on a 12.5% polyacrylamide SDS PAGE gel. After electrophoresis, gel was stained with Instant Blue Protein Stain (Expedeon Protein Solutions).

Mitochondrial activity

Mitochondrial functions were analyzed in differentiated C2C12 cells by a Seahorse XF96 Extracellular Flux Analyzer (Agilent Technologies, UK) following manufacturer's instructions. Briefly, C2C12 myotubes, seeded in XFe96 cell culture microplates (Agilent Technologies) and transfected with siRNA directed against Nrf1, GR, Myod1 or a control siRNA, were incubated with Seahorse XF assay media [25 mM glucose, 1 mM pyruvate and 2 mM glutamine (Agilent)] at 37°C in a CO_2 free incubator for 1 h prior the experiment. The variations in Oxygen Consumption Rate (OCR, pmol/min) were recorded after the sequential addition of oligomycin (ATP synthase inhibitor, 1 μM; Sigma-Aldrich), carbonyl cyanide m-chlorophenylhydrazine (FCCP; mitochondrial uncoupling, 2 μM; Sigma-Aldrich) and Rotenone (complex I inhibitor, 0.5 μM; Sigma-Aldrich) in combination with antimycin A (complex III inhibitor, 0.5 μM; Sigma-Aldrich). OCR values were further normalized to protein content in individual wells using Bradford Reagent (ab119216, Abcam). Basal and maximal respirations were calculated following manufacturer's instructions.

Native polyacrylamide gel analysis

Oligonucleotides (Supplementary Table S5) were annealed at 1 mM in 10 mM Tris–HCl pH 8.0, 100 mM NaCl, and 0.1 mM EDTA, and incubated with purified recombinant GR DBD in a 1:1.2 protein dimer:DNA molar ratio as described (51). GR DBD–DNA complexes were loaded on an 8% native poly-acrylamide gel, run in TBE buffer [89 mM Tris base, 89 mM boric acid (pH 8.3), and 2 mM EDTA-Na_2] and stained with Instant Blue Protein Stain (Expedeon Protein Solutions).

Quantification and statistical analysis

Data are represented as mean + SEM. Significance was calculated with GraphPad Prism (www.graphpad.com, GraphPad Software) using:

(1) two-tailed Student's t test for Figures 2H, 3D–G, I, J, 4E, 5F–H, Supplementary Figures S2H, P, S3B–D, F, I–L, S4E, G, I–K, S5F, H–N;
(2) one-way ANOVA for Figures 5I, 7E, F, Supplementary Figures S7F, H;
(3) two-way ANOVA for Figure 3H, Supplementary Figures S3G, H, M, S4F, S7G.

RESULTS

Identification and characterization of skeletal muscle-specific enhancer regions

To characterize the mechanisms underlying gene transcription in skeletal muscle, we performed genome-wide stud-

ies. Transcriptome analysis of mouse gastrocnemius muscles by RNA sequencing (RNA-seq) detected almost 11 000 transcribed genes (RNA-seq read counts above 50) (Supplementary Figure S1A). To identify cis-regulatory elements, we performed a chromatin immunoprecipitation assay, followed by massive parallel sequencing (ChIP-seq) using an antibody directed against histone H3 acetylated at lysine 27 (H3K27ac), which is present at both active promoters and enhancers (52). We identified 21 377 peaks distributed at intronic and intergenic regions, as well as around the transcription start site (TSS, −1000 bp; +100 bp, Supplementary Figure S1B). Bedtools analysis using the TSS coordinates revealed that 94% of skeletal muscle expressed genes exhibit at least one H3K27ac peak within their promoter region defined as ±1 kb from TSS (Supplementary Figure S1A and Supplementary Table S6), whereas only 10% of the non-expressed genes were positive for this histone mark (Supplementary Figure S1A and Supplementary Table S7). Thus, the presence of H3K27ac is a relevant predictor for active transcription in skeletal muscles. To identify open regulatory regions, we performed transposase-accessible chromatin profiling (ATAC-seq) and identified 67 218 peaks, mainly located at intergenic and intronic regions (Supplementary Figure S1B), with 80% located between 5 and 500 kb from the TSS and a median value of about 50 kb (Supplementary Figure S1C). In addition, ATAC-seq signals strongly correlated with those of H3K27ac (Figure 1A), and 90% of the expressed genes with H3K27ac peaks at the promoter region also had an ATAC-seq peak within a window of 50 kb around the TSS (Supplementary Figure S1D and Supplementary Table S6).

To further characterize the chromatin landscape in skeletal muscles, we performed ChIP-seq analyses of additional histone marks. We identified ~75 000 peaks for H3 monomethylated at lysine 4 [H3K4me1, a chromatin hallmark of enhancers (53)], ~19 000 for H3 trimethylated at lysine 4 [H3K4me3, a mark enriched at promoter regions (53)] and ~13 000 for the RNA polymerase II (Polr2) (Supplementary Figure S1E). We unveiled ~14 000 active promoter regions defined by the presence of H3K27ac, H3K4me3 and Polr2, and low H3K4me1 levels, as well as ~27 000 active enhancer regions defined by the presence of H3K27ac, H3K4me1 and Polr2, and low H3K4me3 levels (Figure 1B and C). Note that 70% of genes, the TSS of which is associated with at least one peak of H3K27ac, H3K4me3, H3K4me1 and Polr2, are transcribed (Supplementary Figure S1F). The identified promoters and enhancers were devoid of the H3K27me3 repressive mark (Figure 1B, C and Supplementary Figure S1E) and were strongly associated with the presence of ATAC-seq peaks (Supplementary Figure S1G), demonstrating that most of them are located in open-chromatin regions, in contrast to non-transcribed genes (Supplementary Figure S1G). To determine whether the identified skeletal muscle enhancers are tissue-specific, we extended our analysis to murine prostatic (54), adipose (55) and hepatic tissues (56) (Supplementary Figure S1H), and revealed 13 200 active enhancers in prostate, 23 500 in adipose tissue and 19 400 in liver (Supplementary Table S8). Remarkably, only 10% of the identified enhancer regions were common across tissues, whereas the remaining clusters were remarkably tissue-specific (Figure 1D and E).

Next, we questioned which transcription factors might be recruited to the skeletal muscle genomic regions identified in Figure 1B. Known motif search using hypergeometric optimization of motif enrichment (HOMER, http://homer.ucsd.edu/homer/) analysis revealed that promoter regions were essentially characterized by repetitive DNA elements (Figure 1F), whereas enhancer regions featured binding sequences for the transcription factors ZNF416 (Zfp418 in mouse, 29%), Tfap4 (26%), Myod1 (18%), and the progesterone receptor (PR; NR3C3 39%), as well as androgen receptor (AR; NR3C4) half-site motifs (61%) (Figure 1G). The normalized gene expression obtained from RNA-seq data showed that Myod1 is the most expressed among these factors in skeletal muscles (Figure 1H). Taking advantage of available Myod1 ChIP-seq datasets in myotubes (57–59), we found that half of the muscle-specific enhancers were bound by Myod1 in myotubes (Figure 1I and J). In contrast, prostate-specific enhancers were mainly associated with ERG and SIX2 motifs, whereas PPAR (NR1C) and RXR (NR2B1) motifs were found at enhancers identified in adipose tissue, and ERRa (NR3B1) and THRb (NR1A2) were predominant in liver (Supplementary Figure S1I). Thus, most active enhancers in skeletal muscle encompass binding sites for transcription factors distinct from those identified in prostate, adipose tissue and liver.

GR is located at active enhancers in skeletal muscles

To characterize skeletal muscle-specific enhancers in more details, we determined AR cistrome by ChIP-seq. Only 584 peaks that were not correlated with the presence of enhancer or promoter marks were obtained (Supplementary Figure S2A and S2B). Note that Western blot analyses revealed that AR levels are at least 10-times lower in muscles than in prostate, a key androgen responsive tissue (Supplementary Figure S2C), indicating that only few skeletal muscle enhancer-containing putative AR binding elements are bound by AR.

Phylogenetic studies have shown that AR, the mineralocorticoid receptor (MR/NR3C2), the progesterone receptor (PR), and the glucocorticoid receptor (GR) form the oxosteroid nuclear receptor subfamily (60). These receptors are liganded by natural 3-ketosteroids and bind as homodimers similar DNA segments composed of two 5′-RGAACA-3′ palindromic half-sites separated by 3 bps (inverted repeat IR3) (61). Interestingly, in skeletal muscles, GR was almost 10-times more expressed than AR, MR and PR (Figure 2A).

Although numerous studies have identified GR binding profiles upon treatment with high doses of synthetic agonists (e.g. dexamethasone), the GR cistrome in skeletal muscles at endogenous glucocorticoid levels remained unknown. Therefore, we carried out a genome-wide GR chromatin occupancy study in mouse limb muscles and unraveled 23 196 high-confidence peaks (Supplementary Figure S2A). Importantly, GR was bound to half of the skeletal muscle-specific enhancers (Figure 2B and C). Additionally, by profiling GR peaks with the other chromatin-binding and epigenomic markers, we observed that GR is
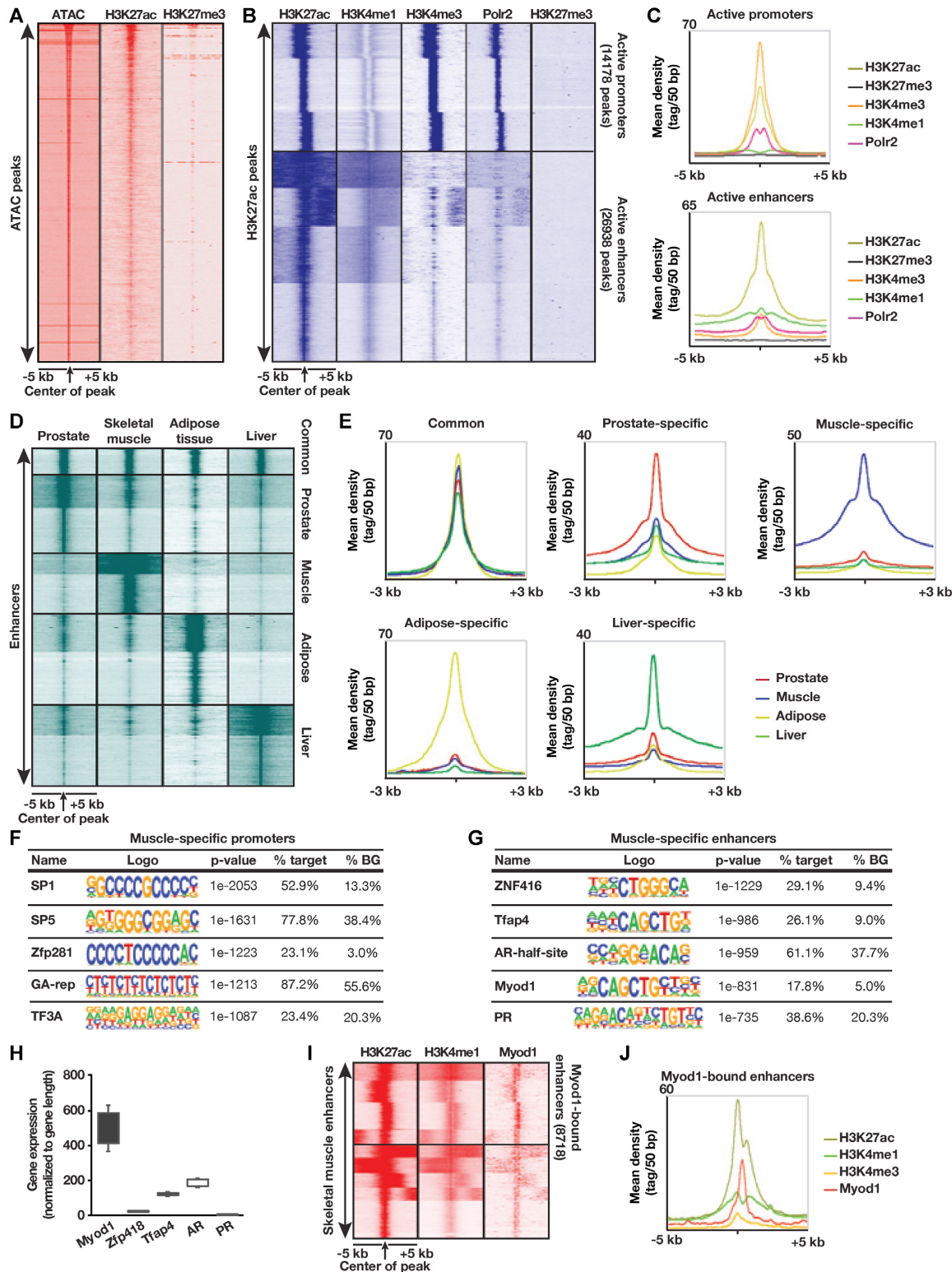
Figure 1. Characterization of mouse skeletal muscle enhancers. (**A**) Tag density map of mouse skeletal muscle ATAC, H3K27ac and H3K27me3 locations, ±5 kb from the ATAC-seq peak center. (**B**, **C**) Tag density map of mouse skeletal muscle H3K27ac, H3K4me1, H3K4me3, H3K27me3 and Polr2 associated locations, ±5 kb from the peak center of H3K27ac (B), and corresponding average tag density profiles of the two identified clusters (C). (**D**, **E**) Tag density map of prostate, skeletal muscle, adipose tissue and liver H3K27ac binding sites, ± 5 kb from the peak center of enhancers identified in these four tissues (D), and corresponding average tag density profiles (E). (**F, G**) HOMER known motif analysis of active promoters (F) and active enhancers (G) in skeletal muscle. BG refers to estimated background. (**H**) Normalized expression of indicated genes in mouse gastrocnemius muscles. (**I, J**) Tag density map of mouse skeletal muscle H3K27ac and H3K4me1, and C2C12 myotube Myod1 binding sites, ±5 kb from the peak center of skeletal muscle enhancers (I), and corresponding average tag density profile of Myod1-bound enhancers (J).
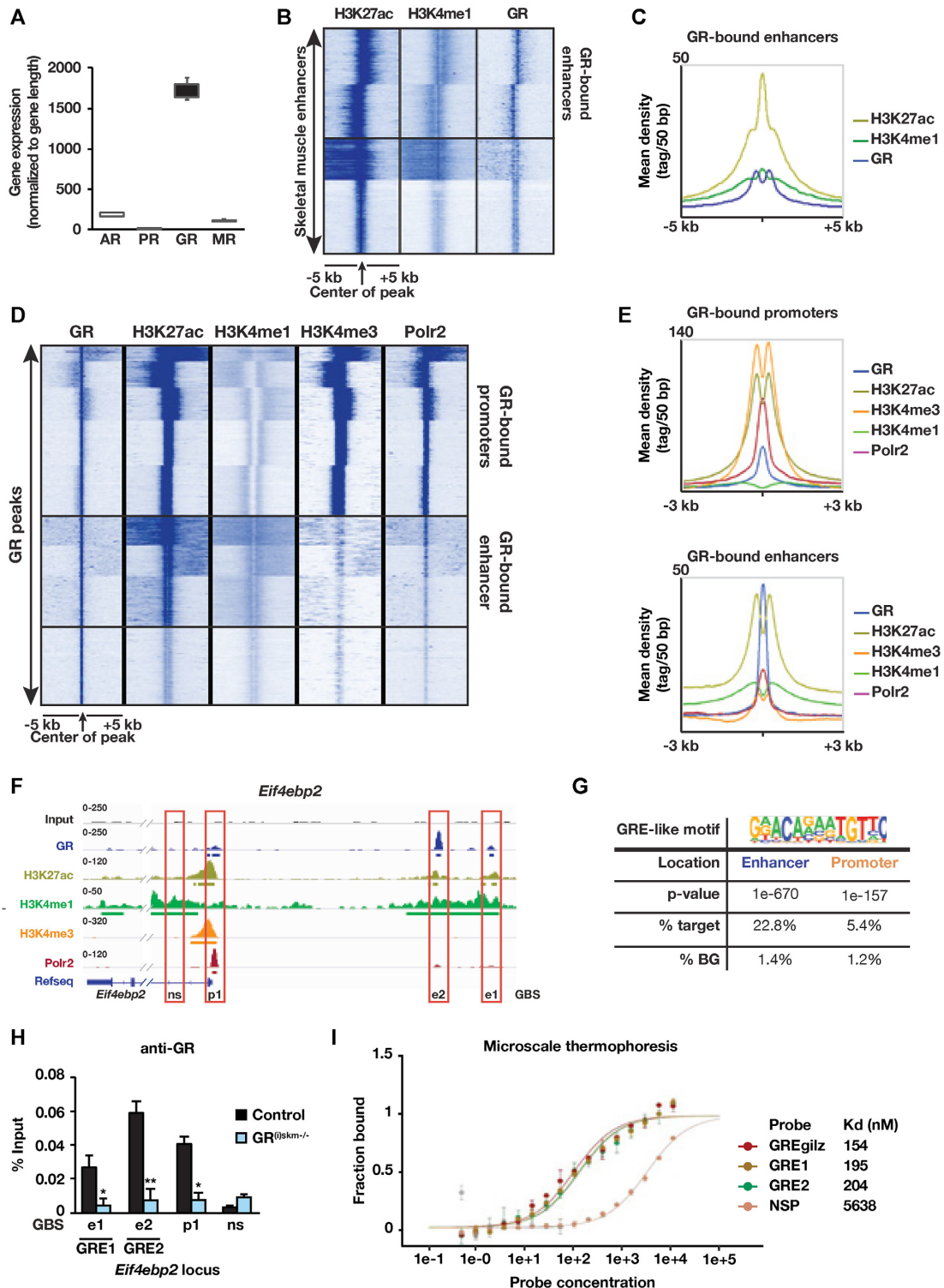
Figure 2. GR binding profile in mouse skeletal muscles. (**A**) Normalized gene expression of indicated genes in mouse gastrocnemius muscles. (**B, C**) Tag density map of mouse skeletal muscle H3K27ac, H3K4me1 and GR binding sites, ±5 kb from the peak center of skeletal muscle-specific enhancers (B), and corresponding average tag density profile of GR-bound enhancers (C). (**D, E**) Tag density map of mouse skeletal muscle GR, H3K27ac, H3K4me1, H3K4me3 and Polr2 binding sites, ±5 kb from the peak center of GR (D), and corresponding average tag density profiles of the two identified clusters (E). (**F**) Localization of GR, H3K27ac, H3K4me1, H3K4me3 and Polr2 at the *Eif4ebp2* locus. The two GR binding sites localized at the enhancer (GBSe1 and GBSe2) and the promoter (GBSp1), and the non-specific binding region (ns) are boxed in red. (**G**) HOMER de novo motif analysis of GR response elements (GREs) peaks located at enhancers and promoter regions. BG refers to estimated background. (**H**) Chromatin immunoprecipitation (ChIP) followed by qPCR analysis (ChIP-qPCR) performed with anti-GR antibodies in skeletal muscle of control and GR$^{(i)skm-/-}$ mice at GBSe1 (GRE1), GBSe2 (GRE2) and GBSp1. The non-specific binding region (ns) depicted in (F) was used as a negative control. $n = 3$ mice. Mean + SEM. *$P < 0.05$; **$P < 0.01$. (**I**) Microscale thermophoresis analysis and corresponding binding affinities of GR DBD to indicated DNA probes.

present at active promoters (∼9500 peaks) and at active enhancers (∼6300 peaks) (Figure 2D). GR peaks reside within nucleosome-free regions within the valley of H3K27ac at both promoter and enhancer regions (Figure 2E), in agreement with the previously described binding profiles of transcription factors (62).

The 23 196 GR binding sites were associated with 11 302 genes, and were equally distributed between the TSS (−1000 bp; +100 bp), intronic, and intergenic locations (Supplementary Figure S2A). Pathway analysis unveiled that the genes bound by GR in skeletal muscles are related to muscle atrophy, including genes of the proteasome system, autophagy, mitophagy, or the Foxo signaling pathway, as well as to metabolism (thermogenesis, thyroid hormone signaling pathway, or fatty liver diseases) and to anabolism (insulin and mTOR signaling pathways) (Supplementary Figure S2D). Various loci of genes involved in these pathways (e.g. *Eif4ebp2*, *Pik3r1*, *Fkbp5*, *Ddit4*, *Ppp1r3c* and *Gadd45g*) are depicted in Figure 2F and Supplementary Figure S2E. HOMER known motif search revealed that GR is bound to 5′-GRACAnnnTGTYC-3′ GRE motifs in >22% of targeted enhancer regions (Figure 2G). In contrast, such motifs were found in only 5% of the GR-bound promoter regions (Figure 2G). Altogether, our data show that GR is bound to a large number of muscle-specific enhancers via GREs.

To identify myofiber-specific GR binding sites, we generated GR$^{(i)skm−/−}$ mice in which GR is selectively ablated in myofibers at adulthood. As expected, GR L2 alleles (Supplementary Figure S2F) were selectively converted into L-alleles in various skeletal muscles of GR$^{(i)skm−/−}$ mutant mice (Supplementary Figure S2G), and GR RNA and protein levels were strongly reduced in these muscles, but not in other tissues (e.g. liver) (Supplementary Figure S2H and S2I). Moreover, immunofluorescent detection of GR protein revealed that GR was efficiently ablated in skeletal muscle fibers, but not in Pax7-positive satellite cells (Supplementary Figure S2J). Sequencing of chromatin isolated from GR$^{(i)skm−/−}$ muscles and immunoprecipitated with GR antibodies uncovered nearly 3 100 peaks, mainly located at introns and intergenic regions (Supplementary Figure S2K), and associated to 2 380 genes. SeqMINER analysis showed that the location of these peaks is distinct from that in wild-type mice (Supplementary Figure S2L), and that only 10% of genes bound by GR in skeletal muscles of WT mice were also bound in those of GR$^{(i)skm−/−}$ mice (Supplementary Figure S2M). Note that GR was no longer recruited to the enhancer region of *Eif4ebp2*, *Pik3r1*, *Fkbp5*, *Ddit4*, *Ppp1r3c* and *Gadd45g* in GR$^{(i)skm−/−}$ muscles (Supplementary Figure S2N). Moreover, HOMER motif search unraveled that sequences below GR binding sites in GR$^{(i)skm−/−}$ muscles do not correspond to GREs, but mainly to bZIP (e.g. Atf, Jun), Hif1b and Smad4 motifs (Supplementary Figure S2O), indicating that GR might tether on various transcription factors in other cell types of the muscle tissue. Together our data show that the recruitment of GR to the identified binding sites in skeletal muscle is largely myofiber-specific.

GR binds with high affinity to both consensus and non-consensus GREs

To further investigate the molecular basis of GR-mediated direct gene activation, we focused on representative enhancer and promoter regions of the translation repressors *Pik3r1* (Supplementary Figure S2E) and *Eif4ebp2* (Figure 2F), which are characterized by long (500 kb) and short (40 kb) 5′-intergenic region, respectively. ChIP-seq analysis revealed two GR-binding sites located at −15.5 and −12.5 kb of the *Eif4ebp2* TSS (GBSe1 and GBSe2, respectively) and one at the promoter region (GBSp1) (Figure 2F). In addition, we identified at least five GREs in the enhancer region of *Pik3r1*, including a close-to-consensus motif (5′-AGAACAtcgTGTTCC-3′, GBSe3; GRE3) 50 kb upstream of the TSS (Supplementary Figure S2E). Interestingly, the sequence of GBSe1 (5′-AGAACActcAGTCCT-3′, GRE1) and GBSe2 (5′-GGTACAcagAGTGCC-3′, GRE2) differed by several nucleotides from the consensus IR3 sequence. ChIP followed by qPCR (ChIP-qPCR) analysis confirmed GR binding to these elements in limb muscles of wild-type mice, whereas almost no amplification was obtained in non-specific regions (ns, Figure 2H and Supplementary Figure S2P). Of note, no GRE-like sequence was identified in GR-bound promoter regions of *Eif4ebp2* (GBSp1, Figure 2F) and of *Pik3r1* (GBSp2, Supplementary Figure S2E), and almost no amplification was detected with chromatin from limb muscles of GR$^{(i)skm−/−}$ mice (Figure 2H, Supplementary Figure S2N and P), demonstrating that GR recruitment to these elements is myofiber-specific.

The *Eif4ebp2* binding site GRE1 is composed of a consensus half-site and a second half-site differing from consensus by two base pairs at positions +2 and +5 (0 being the central base pair of the spacer). Moreover, GRE2 differs from the consensus sequence by two (at positions -5 and -7) and three (at positions +2, +5 and +7) base pairs in the first and in the second half site, respectively. Native polyacrylamide gel analysis revealed that the recombinant human GR DNA binding domain (DBD) formed a complex with the *Gilz* (*Tsc22d3*) GRE (5′-AGAACAttgGGTTCC-3′), a GR response element structurally and functionally characterized in a number of studies (63) (Supplementary Figure S2Q), as well as with GRE1 and GRE2. In contrast, no complexes were formed in the presence of an unrelated probe located in the vicinity of GRE2, or when the base pairs at positions −3 and +3, which were shown to be essential for GR DBD recruitment to DNA (63), were mutated (Supplementary Figure S2Q). To determine the binding affinity of GR DBD to the various DNA segments, we performed microscale thermophoresis (MST) analyses. Whereas the measured dissociation constant (Kd) between GR DBD and either GRE1, GRE2, or GREgilz were similar (195, 204 and 154 nM, respectively; Figure 2I), that of the non-specific probe was at least 30 times above these values. Thus, GR DBD binds with high affinity to the identified non-consensus GREs. Altogether, our data show that myofiber GR binds to consensus and non-consensus GREs at active enhancers, whereas its recruitment to promoters appears to be mainly GRE-independent.

Myofiber GR down-regulates anabolic pathways at physiological glucocorticoid levels

To identify the pathways regulated by myofiber GR at physiological glucocorticoid levels, we performed transcriptome analyses in skeletal muscles, one week after GR ablation. In gastrocnemius muscles, which are mostly composed of fast-twitch muscle fibers (type II), 763 and 1041 genes were up- and down-regulated in GR$^{(i)skm-/-}$ mice, respectively (Figure 3A). Among the down-regulated genes, we found *Fkbp5, Gadd45g, Ppp1r3c, Ddit4* and *Pik3r1* (Figure 3A). Interestingly, in skeletal muscles of control mice, GR was bound to >90% of genes that were downregulated in GR$^{(i)skm-/-}$ mice (Figure 3B). Pathway analysis revealed that direct GR targets encode factors involved in muscle homeostasis, including oxidative metabolism (e.g. fatty acid synthesis and oxidation) and muscle mass regulation (e.g. insulin and PI3K-AKT signaling, myocyte hypertrophy and amino acid metabolism) (Figure 3C). RT-qPCR showed that the levels of anabolic (*Akt3, Rps6kb1* and *Pi3kca*) and anti-anabolic (*Ddit4, Eif4ebp1, Eif4ebp2* and *Pi3kr1*) transcripts were increased and decreased, respectively, upon GR ablation (Figure 3D). Transcriptomic analysis performed in soleus muscle, which is mostly composed of slow type I and IIa fibers, revealed no DEGs between control and GR$^{(i)skm-/-}$ mice with the cropping parameters used for gastrocnemius muscle (*f*-value < 0.025). Note that only 167 genes were down-regulated with a *f*-value <0.05 and a fold-change <0.8, and 276 up-regulated with a *f*-value >0.95 and a fold-change >1.25 (Supplementary Figure S3A), showing that GR mainly contributes to the regulation of gene expression in fast type II fibers.

Interestingly, loss of GR led to an increased mass of gastrocnemius, tibialis and quadriceps limb muscles (Figure 3E, Supplementary Figure S3B and C), which are all mainly composed of fast-twitch fibers. In accordance, the analysis of body mass repartition by quantitative nuclear magnetic resonance (qNMR) revealed a 14% increase in lean mass, but no difference in fat content (Figure 3F). Elevated muscle mass led to a 5−13.5% increased body weight of GR$^{(i)skm-/-}$ mice between 10 and 30 weeks of age (Supplementary Figure S3D). Histological analyses revealed that the number of muscle fibers was similar in 4-month-old control and GR$^{(i)skm-/-}$ mice (Supplementary Figure S3E and F). However, whereas fiber cross sectional area (CSA) distribution was centered around 2000 μm^2 in gastrocnemius muscle of control mice, it was shifted to 2500 μm^2 in that of GR$^{(i)skm-/-}$ mice, resulting in an increased average fiber CSA (Figure 3G and H). Similar shifts in CSA occurred in tibialis and quadriceps muscles (Supplementary Figure S3G−I). Interestingly, limb muscle strength assessed by grip test was increased by 6 and 10% in 4- and 5-month-old GR$^{(i)skm-/-}$ mice, respectively (Figure 3I). Moreover, at 4 months of age, tibialis maximal tetanic force was 24% higher in GR$^{(i)skm-/-}$ mice than in control mice (Figure 3J), whereas its specific force was similar in control and GR$^{(i)skm-/-}$ mice (Supplementary Figure S3J), demonstrating that increased muscle strength results from increased muscle mass. Of note, neither muscle mass nor CSA was affected in soleus muscle (Supplementary Figure S3K−M).

Altogether, these results show that physiological glucocorticoid levels negatively regulate the mass and strength of fast-twitch limb muscles in adult mice by restricting fiber size via myofiber GR.

To determine molecular determinants underlying increased muscle mass and strength in GR$^{(i)skm-/-}$ mice, we performed transcriptome analyses of gastrocnemius muscles at 16 weeks. We found 3264 differentially expressed genes, of which 1834 were up- and 1430 were down-regulated. Pathway analysis revealed that part of down-regulated genes is related to muscle metabolism, including electron transport chain and glucose metabolism (Figure 4A and Supplementary Figure S4A). However, the levels of proteins involved in various OXPHOS sub-complexes and the activity of mitochondrial complex I were not affected upon GR loss (Supplementary Figure S4B and C). Moreover, the analysis of glycogen content determined by Periodic acid–Schiff (PAS) staining (Supplementary Figure S4D), blood glucose levels and glucose uptake (Supplementary Figure S4E and F) showed that glucose metabolism is similar in control and GR$^{(i)skm-/-}$ mice. In addition, cholesterol, triglycerides, free fatty acids and glycerol levels were not affected by loss of GR in myofibers (Supplementary Figure S4G). Altogether, our data show that loss of GR has no major effect on glycolytic and oxidative metabolism in skeletal muscle.

Other genes down-regulated in the absence of GR in myofibers were related to striated muscle contraction, focal adhesion, PI3K-Akt-mTOR-signaling pathway, amino acid metabolism and translation factors (Figure 4A), whereas up-regulated genes were involved in MAPK signaling, insulin signaling and mRNA processing (Figure 4B). The expression levels of genes involved in these pathways are depicted as a heatmap in Figure 4C. In accordance, protein levels of the anabolic factor Akt3 were higher in muscles of GR$^{(i)skm-/-}$ mice, whereas those of anti-anabolic factors Pik3r1, Ddit4, Eif4ebp1 and Eif4ebp2 were strongly decreased, leading to a global activation of the mTOR cascade (Figure 4D and E). As pharmacological levels of glucocorticoids induce muscle catabolic pathways via GR in collaboration with Foxo1 (64), we determined whether GR loss affects this pathway. In the absence of myofiber GR the ratio between phosphorylated and total Foxo1 was decreased (Supplementary Figure S4H−J), indicating that the catabolic pathway might be induced. However, the levels of transcripts encoding various proteins of the proteasome [e.g. Trim63 (Atrogin1) and Fbxo32 (Murf1)], involved in autophagy (e.g. Atg3, Bnip3, Ctsl and Becn1) and calpains (e.g. Capn1 and Capn2) were similar in gastrocnemius muscle of control and GR$^{(i)skm-/-}$ mice (Supplementary Figure S4K). Note that the increased ratio between phosphorylated and total Foxo3a (Supplementary Figure S4H-J) might counteract the decreased Foxo1 ratio.

Together, our data show that myofiber GR impairs the AKT/mTOR signaling pathway by a dual effect on this cascade, since anti-anabolic factors are induced while anabolic factors are reduced, thereby limiting muscle fiber size, without affecting the catabolic cascade.
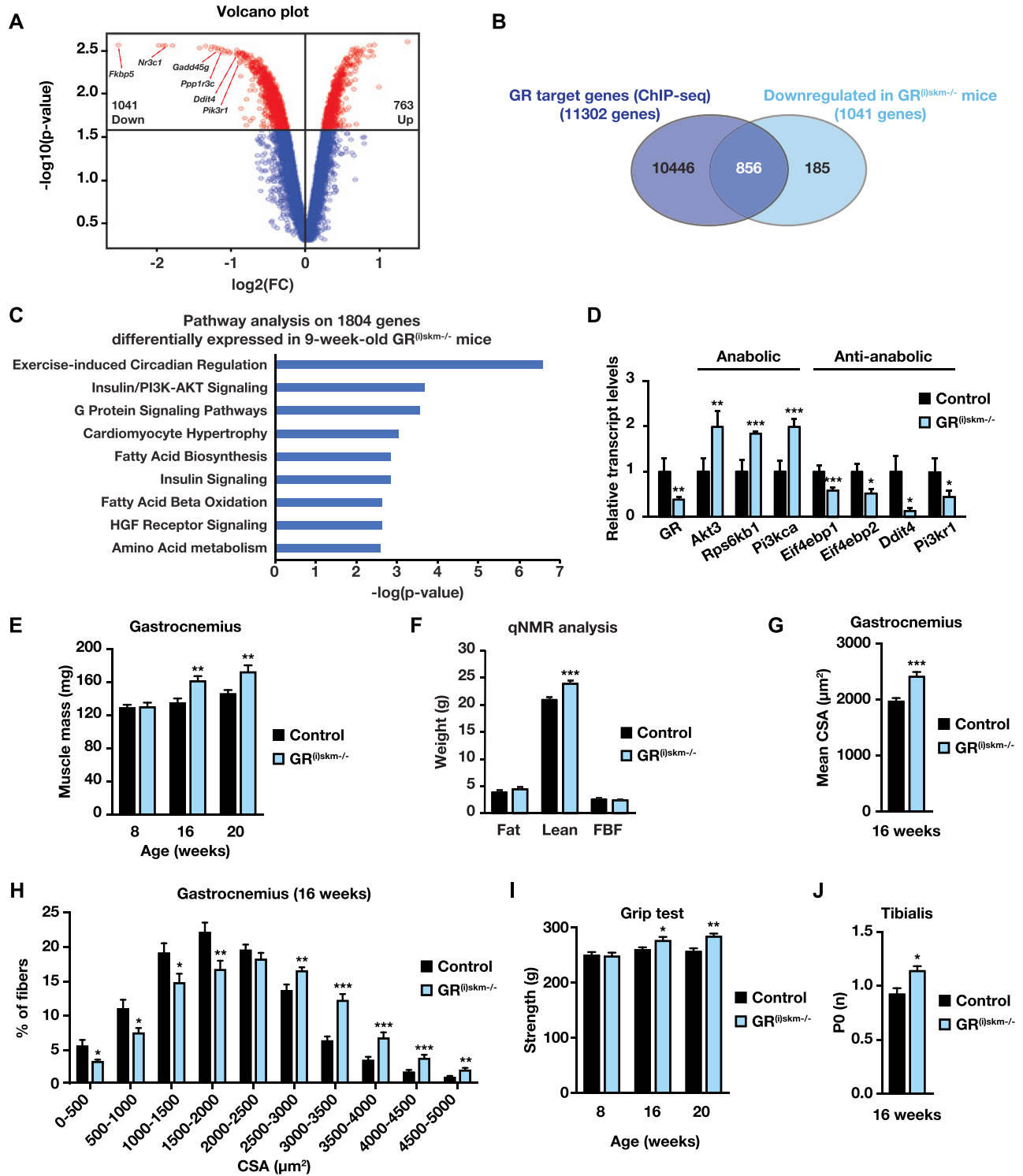
Figure 3. Phenotypic characterization of GR[(i)skm−/−] mice. (**A**) Volcano plot depicting in red genes differentially expressed in gastrocnemius muscles of GR[(i)skm−/−] mice one week after GR ablation. (**B**) Overlap between genes with GR peaks and those down-regulated one week upon GR loss. (**C**) Pathway analysis of up- and down-regulated genes in gastrocnemius muscle of 9-week-old GR[(i)skm−/−] mice. (**D**) Relative transcript levels of representative differentially expressed genes in gastrocnemius muscle of 16-week-old control and GR[(i)skm−/−] mice. (**E**) Mass of gastrocnemius muscle from control and GR[(i)skm−/−] mice at indicated ages. (**F**) qNMR analysis of total fat, lean and free body fluid (FBF) content of 16-week-old control and GR[(i)skm−/−] mice. (**G, H**) Mean cross section area (CSA) (G) and fiber CSA distribution (H) of gastrocnemius muscle from control and GR[(i)skm−/−] mice at 16 weeks. (**I**) Grip strength of 8- to 20-week-old control and GR[(i)skm−/−] mice. (**J**) *In vivo* absolute maximal isometric tetanic force of tibialis anterior muscle from control and GR[(i)skm−/−] mice at 16 weeks. (D−F and I) $n = 10$ mice, (G and H) $n = 4$ mice, (J) $n = 5$. Mean + SEM. *$P < 0.05$; **$P < 0.01$; ***$P < 0.001$.
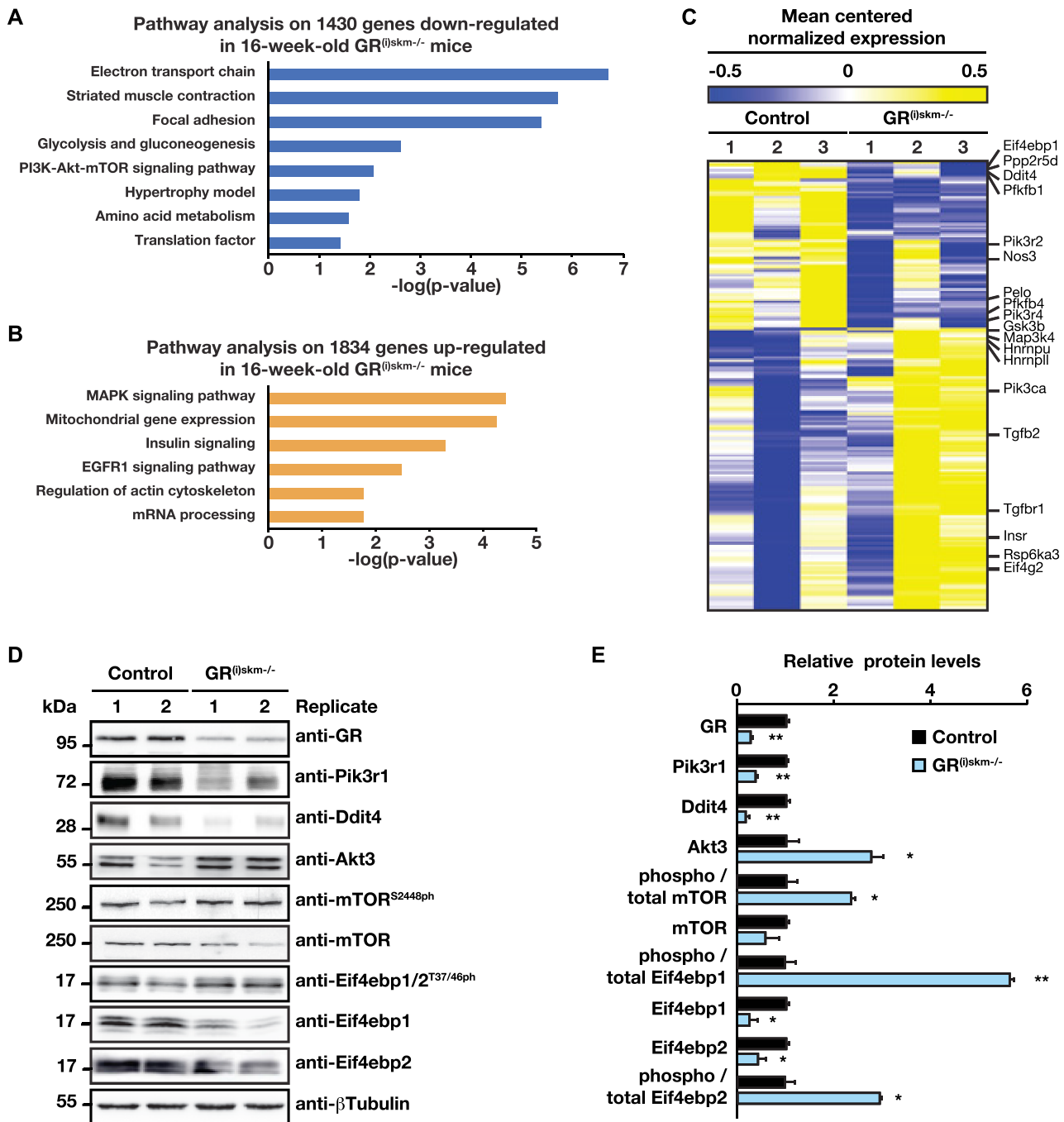
Figure 4. Transcriptomic and protein analyses of gastrocnemius muscles of control and GR$^{(i)skm-/-}$ mice. (**A, B**) Pathway analysis of down- (A) and up- regulated genes (B) in gastrocnemius muscle of 16-week-old GR$^{(i)skm-/-}$ mice. (**C**) Heatmap depicting the mean centered normalized expression of indicated genes selected by pathway analysis from the differentially expressed genes obtained by RNA-seq analysis performed in gastrocnemius muscle of 16-week-old control and GR$^{(i)skm-/-}$ mice. (**D, E**) Representative Western blot analysis (D) and relative levels of the indicated proteins (E) in gastrocnemius muscle of 16-week-old control and GR$^{(i)skm-/-}$ mice. βTubulin was used as a loading control. D, E: $n = 10$ mice. Mean + SEM. *$P < 0.05$, **$P < 0.01$.

GR and Myod1 cooperate to regulate gene transcription in myofibers

Since our data revealed that GR and Myod1 are among the major transcription factors associated with enhancers in skeletal muscles, we questioned whether these factors are functionally intertwined. Motif analyses of GR cistrome revealed that Myod1 E-boxes (5′-CAGCTG-3′) are present in more than 20% of GR-bound enhancers (Figure 5A). Moreover, seqMINER analysis of Myod1 ChIP-seq datasets in myotubes and of GR cistrome in skeletal muscles indicated that Myod1 is bound at one-third of GR peaks (cluster 2, Figure 5B and C). The absence of H3K4me3 associated with the presence of H3K27ac at these shared sites suggested that they are selectively located at enhancers (Fig-
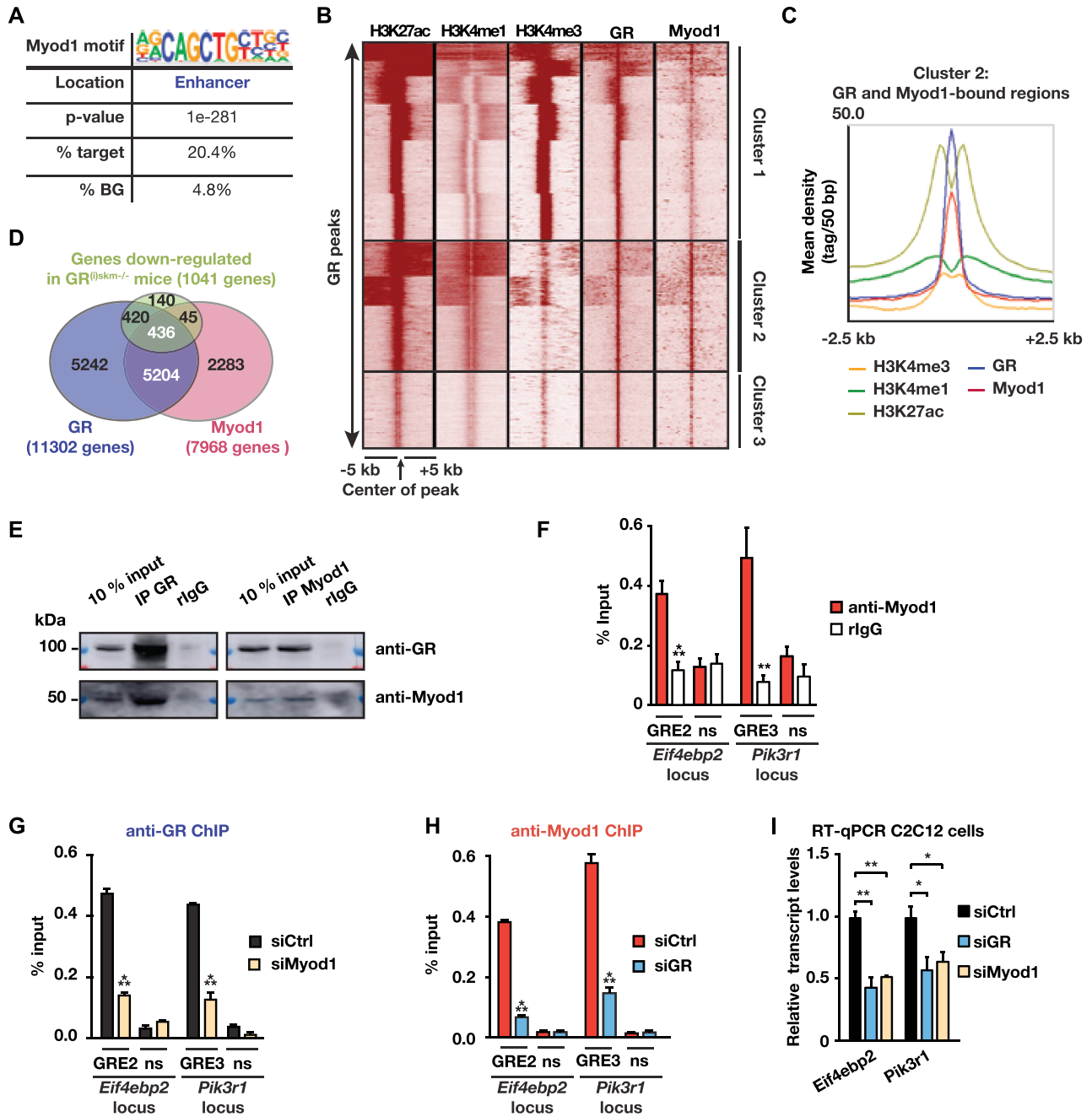
Figure 5. Characterization of Myod1 and GR binding at the *Eif4ebp2* and *Pik3r1* loci. (**A**) HOMER known motif analysis on Myod1 peaks located at GR-bound enhancer regions. BG refers to estimated background. (**B, C**) Tag density map of H3K27ac, H3K4me1, H3K4me3 and GR in skeletal muscles, and Myod1 in C2C12 myotubes, ± 5 kb from the GR peak center (B) and corresponding average tag density profiles of cluster 2 (C). (**D**) Overlap between genes bound by GR in skeletal muscle and by Myod1 in C2C12 myotubes obtained from 3 merged datasets, and genes that are down regulated in GR$^{(i)skm-/-}$ mice. (**E**) Western blot analysis of skeletal muscle nuclear extracts immunoprecipitated with anti-GR or anti-Myod1 antibodies. Membranes were decorated with anti-GR and anti-Myod1 antibodies. rIgG served as a control for immunoprecipitation. Non-immunoprecipitated extracts (10% input) were also analyzed. (**F**) ChIP-qPCR analysis performed at indicated locations with anti-Myod1 antibodies or rIgG in skeletal muscle of wild-type mice. (**G, H**) ChIP-qPCR analysis performed at indicated locations with anti-GR (G) or anti-Myod1 (H) antibodies in C2C12 myotubes transfected with siRNA directed against Myod1 (siMyod1) (G), GR (siGR) (H) or scrambled siRNA (siCtrl). (**I**) Relative *Eif4ebp2* and *Pik3r1* transcript levels determined in C2C12 myotubes transfected with siCtrl, siGR or siMyod1. (F–I): $n = 3$ independent experiments in triplicate. Mean + SEM. $*P < 0.05$; $**P < 0.01$; $***P < 0.001$.

ure 5B). A more detailed quantitative analysis of GR occupancy at enhancers revealed three subsets (Supplementary Figure S5A and B): one to which Myod1 binding is strongly correlated (cluster 1, including those of *Ddit4*, *Gadd45g*, *Mef2a*, *Mt2*, *Pik3r3* and *Tsc22d1*), a second one with a weaker Myod1 signal intensity (cluster 2, including those of *Camk2a*, *Fkbp5* and *Pik3r1*), and a third one in which the binding of GR does not correlate with that of Myod1 (cluster 3). Overall, this analysis shows that 84% of GR-bound enhancers are enriched in Myod1. In addition, the overlap between genes bound by GR in mouse skeletal muscles and those bound by Myod1 in myotubes revealed that Myod1 is recruited to half of the GR target genes (Figure 5D). Moreover, one third of the genes down-regulated in GR$^{(i)skm−/−}$ mice were bound by GR in skeletal muscles from wild-type mice and by Myod1 in myotubes (Figure 5D). Strikingly, co-immunoprecipitation experiments demonstrated that GR and Myod1 interact in skeletal muscles (Figure 5E). To determine whether this interaction is direct, we performed pull-down assay with recombinant full-length GR and Myod1 proteins. GR formed a complex with a polypeptide of its coregulator TIF2, encompassing the nuclear receptor interaction domain (amino acids 623–773), whereas Myod1 did not (Supplementary Figure S5C), indicating that the interaction between GR and Myod1 identified in skeletal muscle is indirect. To validate the recruitment of Myod1 at the enhancer region of *Eif4ebp2* and *Pik3r1* (Supplementary Figure S5D and E), we performed ChIP-qPCR analysis in mouse skeletal muscle nuclear extracts. Myod1 was associated to the DNA segments encompassing GRE2 of *Eif4ebp2* and GRE3 of *Pik3r1*, but not to unrelated region (ns, Figure 5F). In C2C12 myoblasts, Myod1 shares common bind sites with Myog, another E-box binding factor involved in myogenesis (65). However, Myog was expressed at much lower levels in gastrocnemius muscle than in myoblasts, whereas Myod1 levels were similar (Supplementary Figure S5F). Moreover, RNA-seq analysis revealed that Myog is 4 times less expressed than Myod1 in skeletal muscles (Supplementary Figure S5G). In addition, ChIP-qPCR analysis on muscle nuclear extracts showed that Myog was not recruited to the enhancer regions of *Eif4ebp2* and *Pik3r1* (Supplementary Figure S5H).

To further characterize the interplay between GR and Myod1 on gene regulation, we performed small interfering RNA (siRNA)-mediated knock-down of these factors. ChIP-qPCR analysis of C2C12 myotubes transfected with scrambled siRNA showed GR binding to the DNA sequences located in the enhancer regions of *Eif4ebp2* and *Pik3r1* loci identified in skeletal muscles, whereas no DNA was amplified upon GR silencing or from an unrelated region (ns, Supplementary Figure S5I-K). Similarly, Myod1 was recruited to the identified cognate DNA regions of the *Eif4ebp2* and the *Pik3r1* loci, and its binding was abolished after siRNA-mediated knockdown (Supplementary Figure S5L-N). Reduced expression of Myod1 had no effect on GR protein levels (Supplementary Figure S5L), but reduced GR recruitment to its binding sites by at least 50% (Figure 5G). Importantly, GR silencing did not affect Myod1 levels but strongly decreased Myod1 recruitment at *Eif4ebp2* and *Pik3r1* loci (Figure 5H and Supplementary Figure S5I). Moreover, silencing of GR or Myod1 decreased *Eif4ebp2*

and *Pik3r1* transcript levels by about 50% (Figure 5I). Altogether, our data show that GR and Myod1 cooperate at enhancers to control gene expression in skeletal muscles.

GR and Myod1 at enhancers interact with the promoter region of target genes via Nrf1

To determine whether GR and Myod1 located at enhancers interact with the promoter region of their cognate target genes, we performed circular chromosome conformation capture-on-chip associated with high-throughput sequencing (4C-seq) (47) on muscle nuclear extracts. 4C-seq analysis of the *Pik3r1* locus identified >15 upstream domains that interact with the promoter region (viewpoint), whereas no interaction was detected downstream of the TSS (Figure 6A). Interestingly, these upstream regions were marked by H3K4me1 (Figure 6A) that was previously shown to be present at chromatin contact regions (66), and one-third of them was bound by GR via GREs and Myod1 via E-boxes (Figure 6A). Importantly, most of the identified interactions were lost in skeletal muscles of GR$^{(i)skm−/−}$ mice (Figure 6B) and in DP thymocytes (Figure 6C) (27% and 23% left, respectively), indicating that GR-dependent physical enhancer-promoter interactions are tissue/cell-specific.

Strikingly, the genomic DNA segment encompassing the contact domains disclosed by our 4C-seq analysis in skeletal muscle was delimited by two convergent CCCTC-binding factor (Ctcf) binding sites (Figure 6A, Supplementary Figure S6A and B). At these binding sites, the presence of Ctcf was not associated with H3K27ac, H3K4me3 or Myod1, but with H3K4me1 and GR at the gene body of *Pik3r1* (cyan boxes, Figure 6A and Supplementary Figure S6A), and only with H3K4me1 in the upstream region (cyan boxes, Figure 6A and Supplementary Figure S6B). Note that Ctcf was bound to its binding sites in various cell types including DP thymocytes (Supplementary Figure S6C and D), and that these contact domains were present in GR$^{(i)skm−/−}$ mice and DP thymocytes (Figure 6B and C, cyan arrow heads). Thus, TAD formation/maintenance by Ctcf is independent of the establishment of tissue-specific contact domains.

Interestingly, Ctcf was not located at skeletal muscle-specific enhancers *per se* (Figure 7A). Most of them were within a wide window of 20 to 100 kb from the center of these enhancer regions (Supplementary Figure S6E). In addition, >73% of the genes with a Ctcf peak at promoter regions (±5 kb from TSS) had at least one additional Ctcf peak within 100 kb from the TSS. These peaks, located at intergenic regions or within the gene body of neighboring genes, were localized in regions characterized by low active histone marks (Supplementary Figure S7A and B). Note that GR peaks were present in 78% of these 5−100 kb regions, as exemplified in Supplementary Figure S7C, indicating that GR peaks are constrained by Ctcf boundaries. In addition, GR and Myod1 common locations at enhancers did not correlate with the presence of Ctcf, and only a few GR and Ctcf peaks were within the same genomic region (∼ 900 sites), flanked by H3K4me1 (Figure 7B and C). *De novo* motif analysis on these common locations revealed GRE and Ctcf motifs, showing that both factors are bound to their cognate response elements (Supplementary Figure
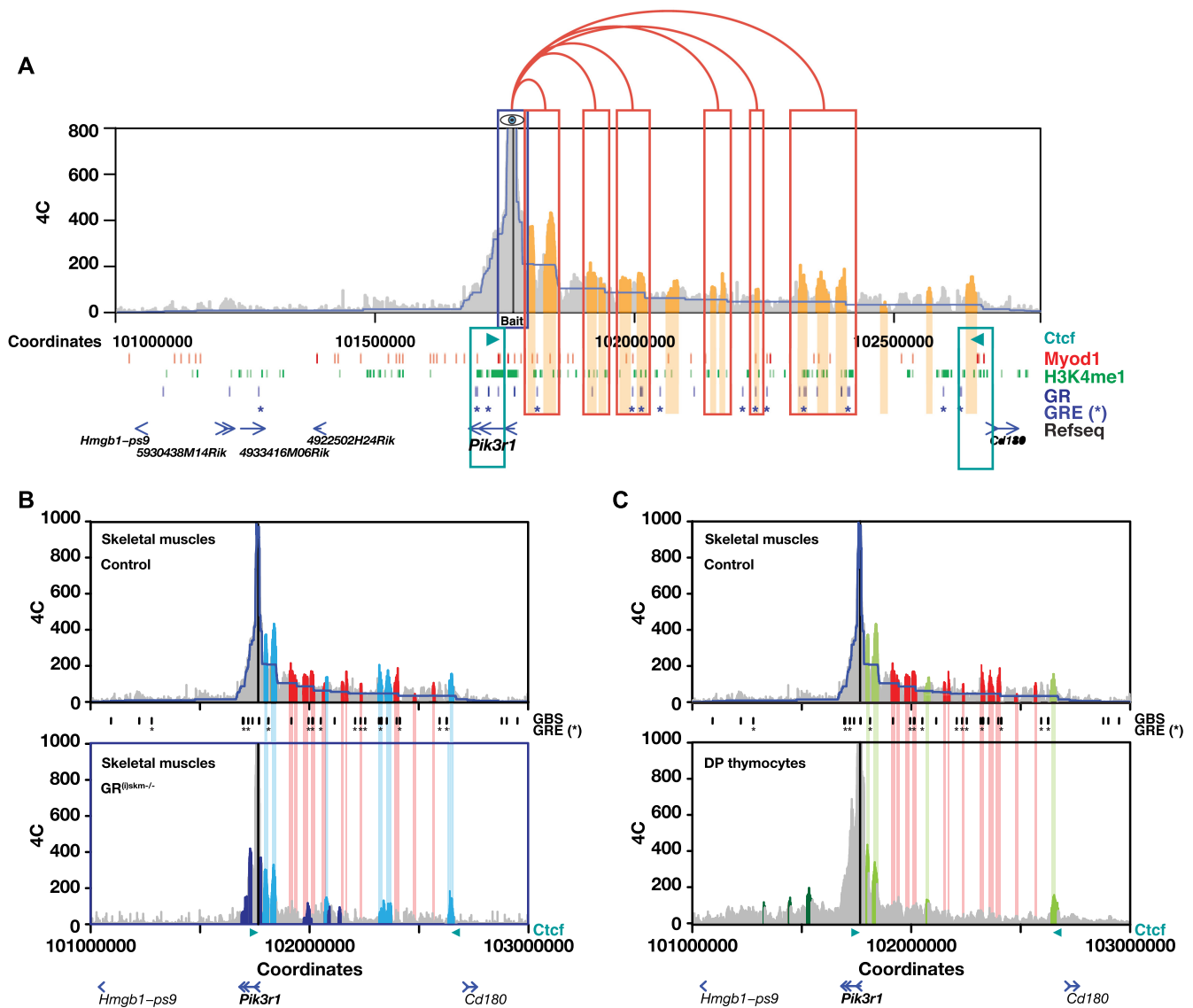
Figure 6. Characterization of *Pik3r1* enhancer-promoter communication. (**A**) Quantitative local 4C-seq signal for the *Pik3r1* viewpoint in skeletal muscle. GR binding sites (GR) are depicted with blue lines, GREs with blue stars, Ctcf binding sites identified by ChIP-seq with cyan arrowheads, indicating convergent motif orientation. H3K4me1 and Myod1 ChIP-seq profiles are presented in green and red, respectively. Enhancer-promoter contact regions are highlighted in orange on the 4C-seq chart. Ctcf-bound promoter and enhancer regions are boxed in cyan. (**B, C**) Quantitative local 4C-seq signal for the *Pik3r1* viewpoint in skeletal muscle of control (upper panels in B and C) mice compared with skeletal muscle GR$^{(i)skm-/-}$ mice (B, lower panel), or with double positive (DP) thymocytes (C, lower panel). Enhancer-promoter contact regions lost upon GR ablation and absent in DP thymocytes are highlighted in red. Contact regions present in both control and GR$^{(i)skm-/-}$ mice are highlighted in light blue. Contact regions present in both control and DP thymocytes are highlighted in light green. Contact regions that are specific for GR$^{(i)skm-/-}$ mice and DP thymocytes are highlighted in dark blue and dark green, respectively. GR binding sites (GBS) are depicted with black lines and GREs with black stars.

S7D). Together, our data show that Ctcf is not located at active enhancers in skeletal muscle, but at H3K4me1-rich regions localized between genes or within the gene body where it frames GR-bound enhancers.

Since our motif analysis revealed that GR is associated to GREs in only 5% of the promoter regions (Figure 2G), we investigated which transcription factors might be bound to the 95% non-GRE-containing segments. *De novo* motif search at GR-occupied promoter regions identified various GC-rich response elements, including the motif of the transcription factor nuclear respiratory factor 1 (Nrf1, 5'-GCGCatGCGC-3') (Figure 7D), that was shown to be recruited to hypomethylated CpG regions (67). ChIP experiments using antibodies directed against GR or Nrf1 followed by qPCR analysis revealed that both transcription factors were recruited to the promoter regions of *Eif4ebp2* (GBSp1) and of *Pik3r1* (GBSp2) (Figure 7E), and that GR recruitment was decreased by 50% upon Nrf1 knockdown (Figure 7F and Supplementary Figure S7E). Of note, GR protein levels and recruitment to the enhancer GRE of *Eif4ebp2* were not affected under these conditions (Figure 7F and Supplementary Figure S7E). Additionally, co-
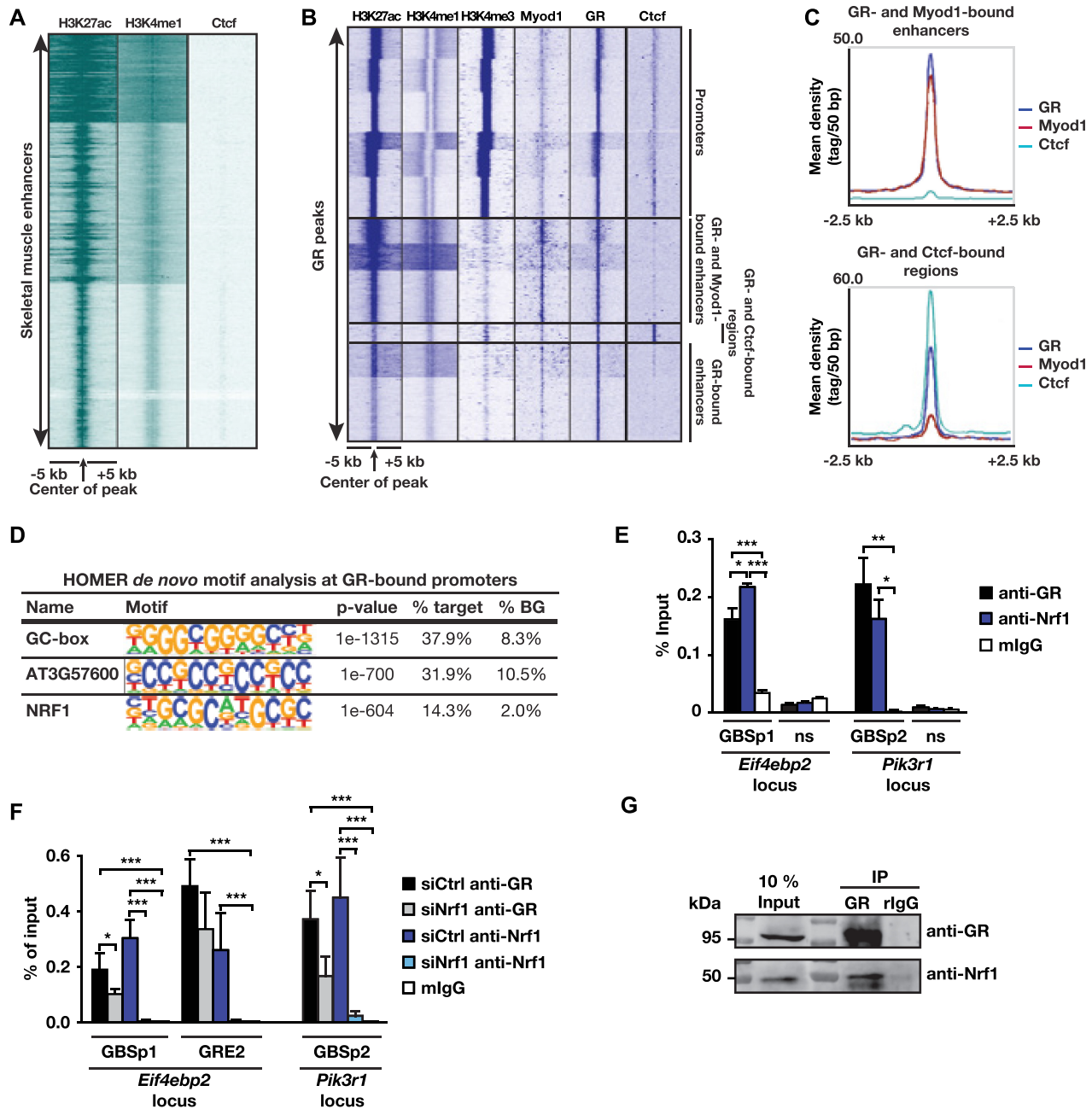
Figure 7. Analysis of enhancer-promoter interactions in skeletal muscle. (**A**) Tag density map of H3K27ac, H3K4me1 and Ctcf, ± 5 kb from center of skeletal muscle-specific enhancers. (**B, C**) Tag density map of H3K27ac, H3K4me1, H3K4me3, GR and Ctcf in skeletal muscles, and of Myod1 in C2C12 myotubes, ± 5 kb from GR peak center (B) and corresponding average tag density profiles of indicated clusters (C). (**D**) HOMER *de novo* motif analysis at GR-bound promoter (−1000 bp to 100 bp) regions. BG refers to estimated background. (**E**) ChIP-qPCR analysis at GR-bound promoter regions of *Eif4ebp2* (GBSp1) and *Pik3r1* (GBSp2), performed with anti-GR, anti-Nrf1 or mouse immunoglobulin G (mIgG) in skeletal muscle of wild-type mice. The non-specific regions (ns) depicted in Supplementary Figure S5D and E were used as a negative control. (**F**) ChIP-qPCR analysis performed at indicated locations with anti-GR or anti-Nrf1 antibodies in C2C12 myotubes transfected with siRNA directed against Nrf1 (siNrf1) or scrambled siRNA (siCtrl). (**G**) Western blot analysis of skeletal muscle nuclear extracts immunoprecipitated (IP) with anti-GR antibodies. Membranes were decorated with anti-GR and anti-Nrf1 antibodies. Rabbit IgG (rIgG) served as a negative control for immunoprecipitation. Non-immunoprecipitated extracts (10% input) were also analyzed. (E, F): $n = 3$ independent experiments in triplicate. Mean + SEM. $*P < 0.05$; $**P < 0.01$; $***P < 0.001$.

immunoprecipitation experiments revealed that Nrf1 and GR interact in muscle nuclear extracts (Figure 7G). Moreover, Nrf1, GR or Myod1 silencing decreased the transcript levels of the GR target genes *Eif4ebp2* and *Pik3r1* by 50% (Supplementary Figure S7F). However, none of these knock-downs affected the expression of *Cytc* and *Uqcrc1*, that were shown to be up-regulated upon NRF1 overexpression (68), or that of various other various nuclear encoded mitochondrial proteins (Supplementary Figure S7E and F). Of note, basal and maximal respirations were lower in Nrf1- and Myod1-silenced myotubes than in control cells, in agreement with previous reports (69) but were not significantly altered by GR loss (Supplementary Figure S7G-H). These data demonstrate the effective role of Nrf1 and Myod1, but not of GR on mitochondrial activity. Altogether, our data show GR and Myod1 at skeletal muscle-specific enhancers interact with Nrf1 located at the promoter region of target genes via the formation of chromatin loops, to stimulate gene transcription.

DISCUSSION

Despite the large number of genome-wide analyses in cellular models, a comprehensive picture of the epigenetic code and intertwined tissue specific-enhancer-bound transcription factors, that confers multicellular organisms their complexity, has remained elusive.

Using distal H3K4me1- and H3K27ac-enriched regions for global enhancer discovery, we identified *cis*-regulatory elements specific for muscle and adipose tissue, prostate and liver. Combining integrative cistromic, epigenomic and transcriptomic analyses, we mapped ∼27 000 skeletal muscle-specific active enhancers, and showed that the motifs to which well-known muscle transcriptional regulators such as Mef2, Nfat or Six bind are not within the first hundred hits at the muscle-specific enhancers, whereas Myod1 and GR are among the most frequent transcription factors bound to enhancers. We found ∼23 000 GR binding sites equally distributed between TSS, intronic, and intergenic locations. Taking advantage of a mouse model in which GR is selectively ablated in myofibers at adulthood, we demonstrate that GR recruitment to these sites is highly myofiber-specific, and coordinates the expression of ∼2000 genes. Moreover, we uncovered additional GR binding sites to those previously identified at the enhancer of *Ddit4* (70) and *Pik3r1* (71). We also found GREs in various anti-anabolic factors, the expression of which is decreased in GR$^{(i)skm-/-}$ mice, leading to an activation of the anabolic Pik3/mTOR pathway. In addition, the transcript levels of numerous genes promoting protein synthesis were increased in skeletal muscles of GR$^{(i)skm-/-}$ mice. Since GR was mainly recruited to the promoter region of the latter genes via DNA sequences for which our bioinformatics analyses did not reveal any consensus motif, we propose that GR might repress the transcription of these genes by tethering to transcription factors that remain to be identified. Moreover, our results show that the mass of fast type-2 muscles is increased in GR$^{(i)skm-/-}$ mice. Thus, physiological glucocorticoid levels exert an anti-anabolic effect in skeletal muscles via myofiber GR.

Former studies have shown that treatments with synthetic glucocorticoids like dexamethasone enhance protein degradation and impair protein synthesis (72) (and references within), leading to muscle atrophy (73,74). In contrast, we show that the expression of genes induced by high glucocorticoid levels and promoting muscle catabolism (74), including the two E3 ubiquitin ligase genes, muscle RING finger 1 (Murf1, Trim63) and muscle atrophy F-box (MAFbx, Fbxo32) (75), was not affected by GR loss, showing that endogenous glucocorticoids via their receptors are not involved in the genomic control of muscle catabolism. As the enhancers of these muscle wasting-related genes were bound by GR at physiological glucocorticoid levels, GR occupancy is not sufficient to affect the transcription of nearby genes. The recruitment of specific co-regulators or DNA-recruited partners might be necessary to ultimately impact the transcription program via the induction of 3D interactions and chromatin looping in new transcriptional regulatory networks. For instance, elevated levels of Foxo1, a known GR partner, are required to synergistically activate the skeletal muscle atrophy-associated genes upon dexamethasone treatment (64).

Importantly, we unraveled a cooperation between GR and Myod1, the latter being recruited to muscle enhancers in a spatially constrained domain centered on GR binding site, in a GR-dependent manner. We show that the presence of Myod1 is also required for GR binding, and that Myod1 contributes to GR-regulated anti-anabolic gene transcription. Thus, Myod1 plays a key role in the muscle fiber-specific GR activities. As former studies identified Myod1 as a myogenic factor (76), it might exert additional functions in myofibers or other cell types (e.g. muscle precursors) by cooperating with other transcription factors.

Our results extend previous Myod1 cistrome characterization in myotubes (57–59), and unravel that the enhancer-specific GR and Myod1 complex bridges distal DNA-regulatory sites to their cognate promoter regions, conferring *cis*-regulatory regions their muscle-specificity and an unequivocal role in the assembly of active gene transcription. We provide evidence that Myod1 and GR induce gene expression mainly through their respective response elements, namely the 5′-CANNTG-3′ E-box and the 5′-RGNACAnnnTGTNCY-3′ glucocorticoid response elements (GREs). Note that such GREs have been previously identified in dexamethasone-treated C2C12 cells (71). Importantly, we show that GR binds with high affinity to GREs that differ from the consensus sequence but at positions −3 and +3, involved in the interaction with the receptor (63). Further analysis combining biophysics and computational approaches are required to determine whether these variations in the binding sequence might impact on receptor activity thereof.

Importantly, our 4C-seq analyses in skeletal muscle reveals that GR and Myod1 are present at contact domains mediating enhancer to promoter connection. As these 3D interactions are reduced in myofiber GR-deficient skeletal muscles and not detected in other cell-types, such as DP thymocytes, GR-regulated enhancer-promoter communications are tissue/cell-specific. In contrast to the cell-specific enhancers, skeletal muscle promoter architecture was not featured by specific transcription factors, but by the pres-

ence of numerous repeated elements including GC-repeats. Remarkably, our cistrome analyses revealed that only 5% of the sites bound by GR at the TSS region contained GREs, whereas a large number encompasses GC-rich sequences, including Nrf1 binding sites. We show that GR interacts with Nrf1 in the nucleus, and that the binding of the latter to its cognate motif contributes to the transcription of GR target genes. Whereas Nrf1 was identified as the key OXPHOS-inducing factor (77), GR loss did not affect the expression of Nrf1 target genes in skeletal muscle. As recent studies proposed that Nrf1 chromatin binding is not tissue-specific, but associated with hypomethylated promoters (67), Nrf1 might facilitate enhancer-promoter communication in collaboration with various enhancer-bound transcription factors.

Our analyses also demonstrate that GR-bound enhancers, topologically associated with Nrf1-bound promoters, are delimited by nested structures of convergent Ctcf sequences. Conversely to the GR and Myod1 common locations at enhancers, Ctcf binding sites were not localized at active enhancers, in contrast with previous studies (78,79), but at H3K4me1-rich regions localized between genes. Ctcf was bound at similar locations in adipocytes, hepatocytes and thymocytes. 4C-seq experiments at the *Pik3r1* locus revealed the presence of a loop framed by convergent Ctcf binding sites in skeletal muscle and in DP-thymocytes. Moreover, additional GR-dependent contact domains were selectively observed in myofibers. Thus, Ctcf recruitment is independent of the activity of cell specific transcription factors, but might be involved in the TAD establishment/maintenance. In contrast, the transcription factor-mediated contact domains residing within this primary loop are likely to contribute to tissue-specific transcriptional activation.

In conclusion, we demonstrate that the cell-specificity arises from dynamic interactions between small sets of transcription factors at regulatory regions. In particular, our results show that collaborative interactions between Myod1, GR and Nrf1 within Ctcf framed genomic regions play a key role in myofiber gene regulation. Moreover, these results unveil the role of physiological glucocorticoid levels in muscle homeostasis. In addition, our data indicate that inhibition of GR in skeletal muscle might provide a new therapeutic option to stimulate anabolic pathways and improve muscle mass and strength of patient affected by muscle wasting even at normo-glucocorticoid levels.

DATA AVAILABILITY

ChIP-seq (GSE14251) and (GSE164543), 4C-seq (GSE142516), ATAC-seq (GSE151790), and RNA-seq (GSE151791) data reported in this study are available at GEO database at https://www.ncbi.nlm.nih.gov/geo/query/acc.cgi?acc=GSE142796, under the accession number GSE142796.

Microarray data are available at GEO database at https://www.ncbi.nlm.nih.gov/geo/query/acc.cgi?acc=GSE144228, under the accession number GSE144228.

Myod1 ChIP-seq datasets were obtained from GSE21621, GSE49313, and GSE56077. H3K27ac, H3K4me1, and H3K4me3 datasets from prostate, adipose tissue, and liver were obtained from GSE47194, GSE58491, and GSE77625, respectively.

The following link was generated to visualise our datasets in UCSC: https://genome.ucsc.edu/s/annabelo23/mm10_GSE142518_UCSC.

SUPPLEMENTARY DATA

Supplementary Data are available at NAR Online.

REFERENCES

1. Dixon,J.R., Selvaraj,S., Yue,F., Kim,A., Li,Y., Shen,Y., Hu,M., Liu,J.S. and Ren,B. (2012) Topological domains in mammalian genomes identified by analysis of chromatin interactions. *Nature*, **485**, 376–380.

2. Hakim,O., John,S., Ling,J.Q., Biddie,S.C., Hoffman,A.R. and Hager,G.L. (2009) Glucocorticoid receptor activation of the Ciz1-Lcn2 locus by long range interactions. *J. Biol. Chem.*, **284**, 6048–6052.

3. Phanstiel,D.H., Van Bortle,K., Spacek,D., Hess,G.T., Shamim,M.S., Machol,I., Love,M.I., Aiden,E.L., Bassik,M.C. and Snyder,M.P. (2017) Static and dynamic DNA loops form AP-1-bound activation hubs during macrophage development. *Mol. Cell*, **67**, 1037–1048.

4. Wang,C., Nanni,L., Novakovic,B., Megchelenbrink,W., Kuznetsova,T., Stunnenberg,H.G., Ceri,S. and Logie,C. (2019) Extensive epigenomic integration of the glucocorticoid response in primary human monocytes and in vitro derived macrophages. *Sci. Rep.*, **9**, 2772.

5. Bonev,B. and Cavalli,G. (2016) Organization and function of the 3D genome. *Nat. Rev. Genet.*, **17**, 772.

6. Hawley,J.A., Lundby,C., Cotter,J.D. and Burke,L.M. (2018) Maximizing cellular adaptation to endurance exercise in skeletal muscle. *Cell Metab.*, **27**, 962–976.

7. Hoffman,E.P. and Nader,G.A. (2004) Balancing muscle hypertrophy and atrophy. *Nat. Med.*, **10**, 584–585.

8. Lecker,S.H., Jagoe,R.T., Gilbert,A., Gomes,M., Baracos,V., Bailey,J., Price,S.R., Mitch,W.E. and Goldberg,A.L. (2004) Multiple types of skeletal muscle atrophy involve a common program of changes in gene expression. *FASEB J.*, **18**, 39–51.

9. An,C.I., Dong,Y. and Hagiwara,N. (2011) Genome-wide mapping of Sox6 binding sites in skeletal muscle reveals both direct and indirect regulation of muscle terminal differentiation by Sox6. *BMC Dev. Biol.*, **11**, 59.

10. Ramachandran,K., Senagolage,M.D., Sommars,M.A., Futtner,C.R., Omura,Y., Allred,A.L. and Barish,G.D. (2019) Dynamic enhancers control skeletal muscle identity and reprogramming. *PLoS Biol.*, **17**, e3000467.

11. Taylor,D.L., Jackson,A.U., Narisu,N., Hemani,G., Erdos,M.R., Chines,P.S., Swift,A., Idol,J., Didion,J.P., Welch,R.P. *et al.* (2019) Integrative analysis of gene expression, DNA methylation, physiological traits, and genetic variation in human skeletal muscle. *Proc. Natl. Acad. Sci. U.S.A.*, **116**, 10883–10888.

12. Williams,K., Ingerslev,L.R., Bork-Jensen,J., Wohlwend,M., Hansen,A.N., Small,L., Ribel-Madsen,R., Astrup,A., Pedersen,O., Auwerx,J. *et al.* (2020) Skeletal muscle enhancer interactions identify genes controlling whole-body metabolism. *Nat. Commun.*, **11**, 2695.

13. Berkes,C.A. and Tapscott,S.J. (2005) MyoD and the transcriptional control of myogenesis. *Semin. Cell Dev. Biol.*, **16**, 585–595.

14. Tapscott,E. (2005) The circuitry of a master switch: Myod and the regulation of skeletal muscle gene transcription. *Development*, **132**, 2685–2695.

15. Fong,A.P., Yao,Z., Zhong,J.W., Cao,Y., Ruzzo,W.L., Gentleman,R.C. and Tapscott,S.J. (2012) Genetic and epigenetic determinants of neurogenesis and myogenesis. *Dev. Cell*, **22**, 721–735.

16. Meijsing,S.H. (2015) Mechanisms of glucocorticoid-regulated gene transcription. *Adv. Exp. Med. Biol.*, **872**, 59–81.

17. Surjit,M., Ganti,K.P., Mukherji,A., Ye,T., Hua,G., Metzger,D., Li,M. and Chambon,P. (2011) Widespread negative response elements mediate direct repression by agonist-liganded glucocorticoid receptor. *Cell*, **145**, 224–241.

18. Schuler,M., Ali,F., Metzger,E., Chambon,P. and Metzger,D. (2005) Temporally controlled targeted somatic mutagenesis in skeletal muscles of the mouse. *Genesis*, **41**, 165–170.

19. Duteil,D., Chambon,C., Ali,F., Malivindi,R., Zoll,J., Kato,S., Geny,B., Chambon,P. and Metzger,D. (2010) The transcriptional coregulators TIF2 and SRC-1 regulate energy homeostasis by modulating mitochondrial respiration in skeletal muscles. *Cell Metab.*, **12**, 496–508.

20. Chambon,C., Duteil,D., Vignaud,A., Ferry,A., Messaddeq,N., Malivindi,R., Kato,S., Chambon,P. and Metzger,D. (2010) Myocytic androgen receptor controls the strength but not the mass of limb muscles. *Proc. Natl. Acad. Sci. U.S.A.*, **107**, 14327–14332.

21. Gali Ramamoorthy,T., Laverny,G., Schlagowski,A.I., Zoll,J., Messaddeq,N., Bornert,J.M., Panza,S., Ferry,A., Geny,B. and Metzger,D. (2015) Mhe transcriptional coregulator PGC-1beta controls mitochondrial function and anti-oxidant defence in skeletal muscles. *Nat. Commun.*, **40**, 10210.

22. Bookout,A.L., Cummins,C.L., Mangelsdorf,D.J., Pesola,J.M. and Kramer,M.F. (2006) High-throughput real-time quantitative reverse transcription PCR. *Curr. Protoc. Mol. Biol.*, doi:10.1002/0471142727.mb1508s73.

23. Livak,K.J. and Schmittgen,T.D. (2001) Analysis of relative gene expression data using real-time quantitative PCR and the 2(-Delta Delta C(T)) Method. *Methods*, **25**, 402–408.

24. Kim,D., Pertea,G., Trapnell,C., Pimentel,H., Kelley,R. and Salzberg,S.L. (2013) TopHat2: accurate alignment of transcriptomes in the presence of insertions, deletions and gene fusions. *Genome Biol.*, **14**, R36.

25. Langmead,B. and Salzberg,S.L. (2012) Fast gapped-read alignment with Bowtie 2. *Nat. Methods*, **9**, 357–359.

26. Anders,S., Pyl,P.T. and Huber,W. (2015) HTSeq–a Python framework to work with high-throughput sequencing data. *Bioinformatics*, **31**, 166–169.

27. Love,M.I., Huber,W. and Anders,S. (2014) Moderated estimation of fold change and dispersion for RNA-seq data with DESeq2. *Genome Biol.*, **15**, 550.

28. Robinson,M.D., McCarthy,D.J. and Smyth,G.K. (2010) edgeR: a bioconductor package for differential expression analysis of digital gene expression data. *Bioinformatics*, **26**, 139–140.

29. Dembele,D. and Kastner,P. (2014) Fold change rank ordering statistics: a new method for detecting differentially expressed genes. *BMC Bioinformatics*, **15**, 14.

30. Dembele,D. and Kastner,P. (2016) Comments on: fold change rank ordering statistics: a new method for detecting differentially expressed genes. *BMC Bioinformatics*, **17**, 462.

31. Wang,J., Duncan,D., Shi,Z. and Zhang,B. (2013) WEB-based GEne SeT AnaLysis Toolkit (WebGestalt): update 2013. *Nucleic Acids Res.*, **41**, W77–W83.

32. de Hoon,M.J., Imoto,S., Nolan,J. and Miyano,S. (2004) Open source clustering software. *Bioinformatics*, **20**, 1453–1454.

33. Saeed,A.I., Bhagabati,N.K., Braisted,J.C., Liang,W., Sharov,V., Howe,E.A., Li,J., Thiagarajan,M., White,J.A. and Quackenbush,J. (2006) TM4 microarray software suite. *Methods Enzymol.*, **411**, 134–193.

34. Joshi,S., Ueberschlag-Pitiot,V., Metzger,D. and Davidson,I. (2017) Improved protocol for chromatin immunoprecipitation from mouse skeletal muscle. *J. Vis. Exp.*, **129**, 56504.

35. Duteil,D., Tosic,M., Lausecker,F., Nenseth,H.Z., Muller,J.M., Urban,S., Willmann,D., Petroll,K., Messaddeq,N., Arrigoni,L. *et al.* (2016) Lsd1 ablation triggers metabolic reprogramming of brown adipose tissue. *Cell Rep.*, **17**, 1008–1021.

36. Zhang,Y., Liu,T., Meyer,C.A., Eeckhoute,J., Johnson,D.S., Bernstein,B.E., Nusbaum,C., Myers,R.M., Brown,M., Li,W. *et al.* (2008) Model-based analysis of ChIP-Seq (MACS). *Genome Biol.*, **9**, R137.

37. Thorvaldsdottir,H., Robinson,J.T. and Mesirov,J.P. (2013) Integrative Genomics Viewer (IGV): high-performance genomics data visualization and exploration. *Brief. Bioinform.*, **14**, 178–192.

38. Heinz,S., Benner,C., Spann,N., Bertolino,E., Lin,Y.C., Laslo,P., Cheng,J.X., Murre,C., Singh,H. and Glass,C.K. (2010) Simple combinations of lineage-determining transcription factors prime cis-regulatory elements required for macrophage and B cell identities. *Mol. Cell*, **38**, 576–589.

39. Ye,T., Krebs,A.R., Choukrallah,M.A., Keime,C., Plewniak,F., Davidson,I. and Tora,L. (2011) seqMINER: an integrated ChIP-seq data interpretation platform. *Nucleic Acids Res.*, **39**, e35.

40. Oliveros,J.C. (2007-2015) Venny. An interactive tool for comparing lists with Venn's diagrams.

41. Heberle,H., Meirelles,G.V., da Silva,F.R., Telles,G.P. and Minghim,R. (2015) InteractiVenn: a web-based tool for the analysis of sets through Venn diagrams. *BMC Bioinformatics*, **16**, 169.

42. Bailey,T.L., Boden,M., Buske,F.A., Frith,M., Grant,C.E., Clementi,L., Ren,J., Li,W.W. and Noble,W.S. (2009) MEME SUITE: tools for motif discovery and searching. *Nucleic Acids Res.*, **37**, W202–W208.

43. Quinlan,A.R. and Hall,I.M. (2010) BEDTools: a flexible suite of utilities for comparing genomic features. *Bioinformatics*, **26**, 841–842.

44. Buenrostro,J.D., Giresi,P.G., Zaba,L.C., Chang,H.Y. and Greenleaf,W.J. (2013) Transposition of native chromatin for fast and sensitive epigenomic profiling of open chromatin, DNA-binding proteins and nucleosome position. *Nat. Methods*, **10**, 1213–1218.

45. Li,H., Handsaker,B., Wysoker,A., Fennell,T., Ruan,J., Homer,N., Marth,G., Abecasis,G., Durbin,R. and Genome Project Data

Processing, S. (2009) The Sequence Alignment/Map format and SAMtools. *Bioinformatics*, **25**, 2078–2079.

46. Ben Zouari,Y., Molitor,A.M., Sikorska,N., Pancaldi,V. and Sexton,T. (2019) ChiCMaxima: a robust and simple pipeline for detection and visualization of chromatin looping in Capture Hi-C. *Genome Biol.*, **20**, 102.

47. van de Werken,H.J., Landan,G., Holwerda,S.J., Hoichman,M., Klous,P., Chachik,R., Splinter,E., Valdes-Quezada,C., Oz,Y., Bouwman,B.A. *et al.* (2012) Robust 4C-seq data analysis to screen for regulatory DNA interactions. *Nat. Methods*, **9**, 969–972.

48. Geeven,G., Teunissen,H., de Laat,W. and de Wit,E. (2018) peakC: a flexible, non-parametric peak calling package for 4C and Capture-C data. *Nucleic Acids Res.*, **46**, e91.

49. Schneider,C.A., Rasband,W.S. and Eliceiri,K.W. (2012) NIH Image to ImageJ: 25 years of image analysis. *Nat. Methods*, **9**, 671–675.

50. Takacs,M., Petoukhov,M.V., Atkinson,R.A., Roblin,P., Ogi,F.X., Demeler,B., Potier,N., Chebaro,Y., Dejaegere,A., Svergun,D.I. *et al.* (2013) The asymmetric binding of PGC-1alpha to the ERRalpha and ERRgamma nuclear receptor homodimers involves a similar recognition mechanism. *PLoS One*, **8**, e67810.

51. Mohideen-Abdul,K., Tazibt,K., Bourguet,M., Hazemann,I., Lebars,I., Takacs,M., Cianferani,S., Klaholz,B.P., Moras,D. and Billas,I.M.L. (2017) Importance of the sequence-directed DNA shape for specific binding site recognition by the estrogen-related receptor. *Front Endocrinol (Lausanne)*, **8**, 140.

52. Creyghton,M.P., Cheng,A.W., Welstead,G.G., Kooistra,T., Carey,B.W., Steine,E.J., Hanna,J., Lodato,M.A., Frampton,G.M., Sharp,P.A. *et al.* (2010) Histone H3K27ac separates active from poised enhancers and predicts developmental state. *Proc. Natl. Acad. Sci. U.S.A.*, **107**, 21931–21936.

53. Sharifi-Zarchi,A., Gerovska,D., Adachi,K., Totonchi,M., Pezeshk,H., Taft,R.J., Scholer,H.R., Chitsaz,H., Sadeghi,M., Baharvand,H. *et al.* (2017) DNA methylation regulates discrimination of enhancers from promoters through a H3K4me1-H3K4me3 seesaw mechanism. *BMC Genomics*, **18**, 964.

54. Pihlajamaa,P., Sahu,B., Lyly,L., Aittomaki,V., Hautaniemi,S. and Janne,O.A. (2014) Tissue-specific pioneer factors associate with androgen receptor cistromes and transcription programs. *EMBO J.*, **33**, 312–326.

55. Kang,S., Tsai,L.T., Zhou,Y., Evertts,A., Xu,S., Griffin,M.J., Issner,R., Whitton,H.J., Garcia,B.A., Epstein,C.B. *et al.* (2015) Identification of nuclear hormone receptor pathways causing insulin resistance by transcriptional and epigenomic analysis. *Nat. Cell Biol.*, **17**, 44–56.

56. Soltis,A.R., Kennedy,N.J., Xin,X., Zhou,F., Ficarro,S.B., Yap,Y.S., Matthews,B.J., Lauffenburger,D.A., White,F.M., Marto,J.A. *et al.* (2017) Hepatic dysfunction caused by consumption of a high-fat diet. *Cell Rep.*, **21**, 3317–3328.

57. Mousavi,K., Zare,H., Dell'orso,S., Grontved,L., Gutierrez-Cruz,G., Derfoul,A., Hager,G.L. and Sartorelli,V. (2013) eRNAs promote transcription by establishing chromatin accessibility at defined genomic loci. *Mol. Cell*, **51**, 606–617.

58. Mullen,A.C., Orlando,D.A., Newman,J.J., Loven,J., Kumar,R.M., Bilodeau,S., Reddy,J., Guenther,M.G., DeKoter,R.P. and Young,R.A. (2011) Master transcription factors determine cell-type-specific responses to TGF-beta signaling. *Cell*, **147**, 565–576.

59. Umansky,K.B., Gruenbaum-Cohen,Y., Tsoory,M., Feldmesser,E., Goldenberg,D., Brenner,O. and Groner,Y. (2015) Runx1 Transcription Factor Is Required for Myoblasts Proliferation during Muscle Regeneration. *PLos Genet.*, **11**, e1005457.

60. Gronemeyer,H., Gustafsson,J.A. and Laudet,V. (2004) Principles for modulation of the nuclear receptor superfamily. *Nat. Rev. Drug Discov.*, **3**, 950–964.

61. Billas,I. and Moras,D. (2013) Allosteric controls of nuclear receptor function in the regulation of transcription. *J. Mol. Biol.*, **425**, 2317–2329.

62. Pundhir,S., Bagger,F.O., Lauridsen,F.B., Rapin,N. and Porse,B.T. (2016) Peak-valley-peak pattern of histone modifications delineates active regulatory elements and their directionality. *Nucleic Acids Res.*, **44**, 4037–4051.

63. Meijsing,S.H., Pufall,M.A., So,A.Y., Bates,D.L., Chen,L. and Yamamoto,K.R. (2009) DNA binding site sequence directs glucocorticoid receptor structure and activity. *Science*, **324**, 407–410.

64. Waddell,D.S., Baehr,L.M., van den Brandt,J., Johnsen,S.A., Reichardt,H.M., Furlow,J.D. and Bodine,S.C. (2008) The glucocorticoid receptor and FOXO1 synergistically activate the skeletal muscle atrophy-associated MuRF1 gene. *Am. J. Physiol. Endocrinol. Metab.*, **295**, E785–E797.

65. Cao,Y., Kumar,R.M., Penn,B.H., Berkes,C.A., Kooperberg,C., Boyer,L.A., Young,R.A. and Tapscott,S.J. (2006) Global and gene-specific analyses show distinct roles for Myod and Myog at a common set of promoters. *EMBO J.*, **25**, 502–511.

66. Yan,J., Chen,S.A., Local,A., Liu,T., Qiu,Y., Dorighi,K.M., Preissl,S., Rivera,C.M., Wang,C., Ye,Z. *et al.* (2018) Histone H3 lysine 4 monomethylation modulates long-range chromatin interactions at enhancers. *Cell Res.*, **28**, 204–220.

67. Domcke,S., Bardet,A.F., Adrian Ginno,P., Hartl,D., Burger,L. and Schubeler,D. (2015) Competition between DNA methylation and transcription factors determines binding of NRF1. *Nature*, **528**, 575–579.

68. Baar,K., Song,Z., Semenkovich,C.F., Jones,T.E., Han,D.H., Nolte,L.A., Ojuka,E.O., Chen,M. and Holloszy,J.O. (2003) Skeletal muscle overexpression of nuclear respiratory factor 1 increases glucose transport capacity. *FASEB J.*, **17**, 1666–1673.

69. Shintaku,J., Peterson,J.M., Talbert,E.E., Gu,J.M., Ladner,K.J., Williams,D.R., Mousavi,K., Wang,R., Sartorelli,V. and Guttridge,D.C. (2016) MyoD regulates skeletal muscle oxidative metabolism cooperatively with alternative NF-kappaB. *Cell Rep.*, **17**, 514–526.

70. Shimizu,N., Yoshikawa,N., Ito,N., Maruyama,T., Suzuki,Y., Takeda,S., Nakae,J., Tagata,Y., Nishitani,S., Takehana,K. *et al.* (2011) Crosstalk between glucocorticoid receptor and nutritional sensor mTOR in skeletal muscle. *Cell Metab.*, **13**, 170–182.

71. Kuo,T., Lew,M.J., Mayba,O., Harris,C.A., Speed,T.P. and Wang,J.C. (2012) Genome-wide analysis of glucocorticoid receptor-binding sites in myotubes identifies gene networks modulating insulin signaling. *Proc. Natl. Acad. Sci. U. S. A.*, **109**, 11160–11165.

72. Watson,M.L., Baehr,L.M., Reichardt,H.M., Tuckermann,J.P., Bodine,S.C. and Furlow,J.D. (2012) A cell-autonomous role for the glucocorticoid receptor in skeletal muscle atrophy induced by systemic glucocorticoid exposure. *Am. J. Physiol. Endocrinol. Metab.*, **302**, E1210–E1220.

73. Ruff,R.L., Martyn,D. and Gordon,A.M. (1982) Glucocorticoid-induced atrophy is not due to impaired excitability of rat muscle. *Am. J. Physiol.*, **243**, E512–521.

74. Schakman,O., Kalista,S., Barbe,C., Loumaye,A. and Thissen,J.P. (2013) Glucocorticoid-induced skeletal muscle atrophy. *Int. J. Biochem. Cell Biol.*, **45**, 2163–2172.

75. Bodine,S.C., Latres,E., Baumhueter,S., Lai,V.K., Nunez,L., Clarke,B.A., Poueymirou,W.T., Panaro,F.J., Na,E., Dharmarajan,K. *et al.* (2001) Identification of ubiquitin ligases required for skeletal muscle atrophy. *Science*, **294**, 1704–1708.

76. Yamamoto,M., Legendre,N.P., Biswas,A.A., Lawton,A., Yamamoto,S., Tajbakhsh,S., Kardon,G. and Goldhamer,D.J. (2018) Loss of MyoD and Myf5 in skeletal muscle stem cells results in altered myogenic programming and failed regeneration. *Stem Cell Rep.*, **10**, 956–969.

77. Ramachandran,B., Yu,G. and Gulick,T. (2008) Nuclear respiratory factor 1 controls myocyte enhancer factor 2A transcription to provide a mechanism for coordinate expression of respiratory chain subunits. *J. Biol. Chem.*, **283**, 11935–11946.

78. Kim,T.H., Abdullaev,Z.K., Smith,A.D., Ching,K.A., Loukinov,D.I., Green,R.D., Zhang,M.Q., Lobanenkov,V.V. and Ren,B. (2007) Analysis of the vertebrate insulator protein CTCF-binding sites in the human genome. *Cell*, **128**, 1231–1245.

79. Shen,Y., Yue,F., McCleary,D.F., Ye,Z., Edsall,L., Kuan,S., Wagner,U., Dixon,J., Lee,L., Lobanenkov,V.V. *et al.* (2012) A map of the cis-regulatory sequences in the mouse genome. *Nature*, **488**, 116–120.